Geomorphology 367 (2020) 107273

Contents lists available at ScienceDirect

Geomorphology

journal homepage: www.elsevier.com/locate/geomorph

Holocene evolution of the Chan May coastal embayment, central Vietnam: Changing coastal dynamics associated with decreasing rates of progradation possibly forced by mid- to late-Holocene sea-level changes

C. Gouramanis [a,*], A.D. Switzer [b,c], C.S. Bristow [d], D.T. Pham [e], B. Mauz [f], Q.D. Hoang [g], D.D. Lam [h], Y.S. Lee [b,c], J.L.A. Soria [b,c], J. Pile [b,c,j], N.T.K. Chi [g], D. Nghiem [g], C. Sloss [i]

[a] Department of Geography, National University of Singapore, 117570, Singapore
[b] Earth Observatory of Singapore, Nanyang Technological University Singapore, 639798, Singapore
[c] Asian School of the Environment, Nanyang Technological University Singapore, 639798, Singapore
[d] Department of Earth and Planetary Sciences, Birkbeck University of London, Malet Street, London WC1E 7HX, UK
[e] VNU University of Science, Vietnam National University, Hanoi, Viet Nam
[f] School of Environmental Sciences, University of Liverpool, United Kingdom
[g] Hanoi University of Mining and Geology, Hanoi, Viet Nam
[h] Institute of Geological Sciences, Vietnam Academy of Science and Technology, 84, Chua Lang, Dong Da, Hanoi, Viet Nam
[i] School of Earth and Atmospheric Science, Queensalnd University of Technology, Brisbane 4001, Australia
[j] Environment Agency, Iceni House, Ipswich, IP3 9JD, UK

ARTICLE INFO

Article history:
Received 14 October 2019
Received in revised form 21 May 2020
Accepted 26 May 2020
Available online 29 May 2020

Keywords:
Ground Penetrating Radar
Quartz optical stimulated luminescence dating
Typhoon
Sea level

ABSTRACT

Southeast Asian coastal environments are undergoing massive transformations with unprecedented population and infrastructure development. These transformations are occurring on a backdrop of intense natural and anthropogenic environmental change, which are increasing the risk to the burgeoning coastal population. Little is known about how central Vietnamese coastal environments have changed naturally since the mid-Holocene sea-level highstand and how recent anthropogenic change and sea-level variation have affected the coastal system. The Chan May embayment in central Vietnam allows us to examine how recent changes in both anthropogenic development and sea-level change have affected the coastline. The embayment preserves a series of prograding beach ridges and is subject to intense human pressures with the construction of a large economic and industrial park, and expansion of tourist facilities. Using ground penetrating radar and quartz optical dating we identify a switch from 6000 years of prograding beach ridges to transgressive dunes within the past century resulting in a decreasing rate of beach ridge progradation possibly in the last 100 years. The recent modes of sediment deposition through washovers and a transgressive dune indicates that coastal progradation has slowed and might have stopped.

1. Introduction

Coastal populations have been growing at an unprecedented rate over the last few decades (e.g., Neumann et al., 2015) resulting in an intensified infrastructure development and exploitation of coastal ecosystems (e.g. Sánchez-Arcilla et al., 2016). In Southeast Asia, this intensification has had profound effects on the coastal environment as major infrastructure projects have frequently been undertaken with little understanding of the environments being developed (e.g. Hoang, 2012), or the ramifications for developing coastal environments in light of future sea-level rise (Jevrejeva et al., 2016) and the impacts of coastal hazards (e.g. Pile et al., 2018).

The impacts of coastal development are particularly important in coastal Vietnam where extensive land use change and environmental modification has occurred over the last three decades along much of the coastline (e.g. Hoang, 2012). To facilitate the promotion of environmentally sustainable development in coastal environments, local- and regional-scale knowledge of the long-term natural processes and what drivers influence those processes must be gained in each region. One method for evaluating changes in natural processes is to compare and contrast the processes of the past with those that are shaping the environment today. The examination of Holocene palaeoenvironments in coastal settings provides valuable insights into the long term environmental changes, such as sea-level variability (e.g. Nielsen et al., 2017) and changing sediment supply (e.g. Taylor and Stone, 1996; Tamura,

* Corresponding author.
E-mail address: geogc@nus.edu.sg (C. Gouramanis).

https://doi.org/10.1016/j.geomorph.2020.107273
0169-555X/

2012), but can also provide records of hazards, such as storms (e.g. Cunningham et al., 2011) and tsunami (e.g. Simms et al., 2017; Gouramanis et al., 2015).

Coastal environments of central Vietnam have received little attention when compared to the intensely investigated Red River Delta in the north (e.g. Tanabe et al., 2006; Tanaka et al., 2011; Thao et al., 2013) and the Mekong River Delta in the south (e.g. Nguyen et al., 2000, 2010; Ta et al., 2005; Tamura et al., 2012). Addressing this knowledge gap is important as central Vietnam is becoming an increasingly popular destination for local and foreign tourists, contains Vietnam's third largest city (Danang), contains iconic and globally-significant environmental, historic and culturally-important sites, and is rapidly becoming an economic hub with intense local and foreign investment (Hayton, 2010; Hoang, 2012; Goscha, 2016).

The regional sea-level trend shows a rapid rise in the early Holocene (Hanebuth et al., 2000; Ta et al., 2002; Schimanski and Stattegger, 2005), peaking at ca. 5 m above present mean sea level (pmsl; Hanebuth et al., 2000) and between ca. 2 and 4 m above pmsl (Ta et al., 2002). From offshore seismic profiles, Schimanski and Stattegger (2005) determined very high rates of Holocene fluvial sedimentation supply to the shelf (50–100 cm/ky), that resulted in significant subsidence of the central section of the Vietnamese continental shelf, and by extrapolation, a different sea-level curve for the central portion of the Vietnamese coastline. The low-lying coastal area of central Vietnam is also under serious threat of inundation and contamination of fresh groundwater from projected sea-level rise, and the potential threat of tsunami inundation (Hoang, 2012).

More recently, the complex and dynamic interactions between accelerated anthropogenic impacts, such as rapid infrastructure development (e.g. Neumann et al., 2015), population growth (e.g. Sánchez-Arcilla et al., 2016) and sea-level change (e.g. IPCC, 2019), and the impacts of coastal hazards requires a detailed examination to sustainably manage infrastructure development and coastal communities.

As such, this study provides a detailed examination into the Holocene coastal landscape evolution of the Chan May embayment, in central Vietnam. The relatively small and centrally located Chan May embayment serves as an important corollary and model for coastal evolution in similarly narrow, non-deltaic continental coastal plains bordered by high and steep terrains. The location also serves as a key site for examining coastal changes in data-poor central Vietnam. We use Ground Penetrating Radar (GPR) and quartz optical stimulated luminescence (OSL) dating to reconstruct the palaeoenvironmental history of the embayment. These techniques, allow us to examine slow processes and short-lived catastrophic events to contextualise the dynamic nature of this coastal system.

2. Background

2.1. Beach ridge records of environmental change

Beach-ridge plains typically develop in areas where the sediment supply to the coast outpaces accommodation space, typically occurring when the sea level is stable or falling (e.g. Taylor and Stone, 1996; Otvos, 2000; Tamura, 2012). Beach ridges can be modified after an erosive event when sediments are removed from the coast and stored as bars in the offshore environment. Upon cessation of the erosive event, fair weather waves redistribute the sediment back into the newly created accommodation space through onshore migrating swash bars, and so rebuild the beach. Above the strandline, foredunes are built through the accumulation of sand reworked by aeolian processes and subsequently vegetated. The entire aeolian and wave-built structure is a beach ridge then builds seaward (e.g. Taylor and Stone, 1996; Tamura, 2012; Tamura et al., 2018, 2019a; Nott, 2019). As such, individual beach ridge sequences can preserve evidence of relatively slow processes such as sea-level change (e.g. Nielsen et al., 2017; Sloss et al., 2018), and/or punctuated episodes of coastal change (storms and tsunami; e.g. Buynevich et al., 2007; Cunningham et al., 2011; Simms et al., 2017; Tamura et al., 2018, 2019a; Nott et al., 2013; Nott, 2019).

2.2. Ground penetrating radar (GPR)

Ground penetrating radar (GPR), coupled with high-resolution topography, is a common technique for evaluating the subsurface stratigraphy in sandy coastal environments (e.g. Jol and Bristow, 2003; Neal, 2004; Mallinson et al., 2011, 2014; Switzer et al., 2020). Typically, GPR data are collected by sequentially pulsing high-frequency radio waves into the ground along a measured profile. Each electromagnetic pulse propagates into the subsurface and interacts with the underlying sediments. As the electromagnetic waves interact with the sediments, variation in the dielectric field causes some of the energy to be reflected back to the surface where the GPR measures the time and strength of the returning signal.

The reflected electromagnetic signal also varies in strength due to subtle or pronounced differences in the subsurface character of the sediments. The subsurface variation may be due to stratigraphy, sediments, mineralogy, water content and hydrogeochemistry. As such, the collection of long, semi-continuous transects of GPR data facilitates the interpretation of the subsurface reflected electromagnetic environment, termed radar facies, and this in turn allows the interpretation of subsurface stratigraphy (Jol and Bristow, 2003; Neal, 2004; Mallinson et al., 2014; Pile et al., 2019; Switzer et al., 2020).

3. The Chan May embayment

3.1. Geomorphology

The Chan May embayment is located 35 km north of Danang and 45 km southeast of Hue in central Vietnam. The embayment is relatively small when compared with the embayments to the north and south (Fig. 1). The shallowly-dipping (1.33°), 5-km–long, east-west beachfront is backed by an extensive beach ridge plain that extends >11 km from the current shoreline to the steep, granitic, heavily-forested, Precambrian Truong Son Range (Fig. 1). The Truong Son Range encloses the embayment along the western and southern margins and most of the eastern margin (Fig. 1; Sterling et al., 2006).

The embayment itself is broadly separated into two components, a narrower (approximately 4.5 km wide) inland embayment consisting of north-northwest to south-southeast trending beach ridges and a wider (approximately 6.5 km wide) northerly embayment consisting of east to west trending beach ridges (Fig. 1). There is no evidence to suggest that the beach ridges in these sub-embayments are discontinuous, but the beach ridge sequence is traversed by a wide (500–1000 m) floodplain and 2.1 km long scroll bar sequence formed by the past flow of the Bulu River (Fig. 1). The headwaters of the Bulu River have also recently (2014–2016) been dammed for freshwater storage and consumption by the local communities.

At present, several small townships occur throughout the Chan May embayment but recent major infrastructure include the construction of a deep water port and port facilities, numerous large arterial roads and an interstate railway as part of the 2025 Economic Master Plan for the region (TPCTTHP, n.d.).

3.2. Climate, nearshore oceanography and recent typhoons

Central Vietnam generally experiences a distinctive monsoon climate with considerable local variability in relation to elevation and proximity to the coast. At Danang, the annual average precipitation and temperature is 1935 mm/yr (from 24 years of complete data) and 25.8 ± 0.4 °C (from 44 years of complete data). Between 1978 and 1989, Lang Co recorded average annual precipitation of 2245 mm/yr, in contrast to the high elevation Bach Ma station that recorded 7977 mm/yr (data spanning from 1932 to 1935; Nghiem, 2009).

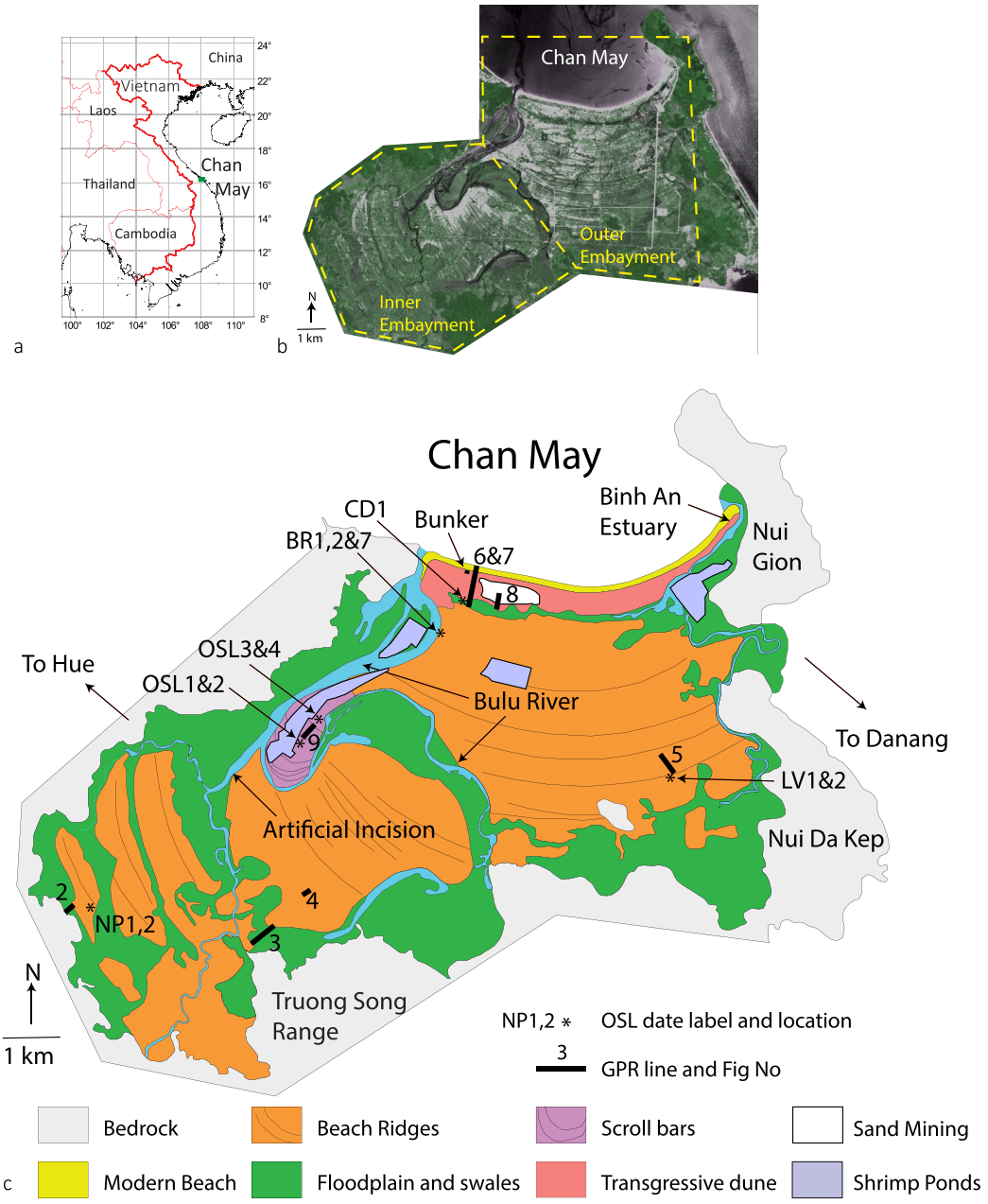

Fig. 1. A) Location of the Chan May embayment; b) 2012 GeoEye satellite image of the Chan May embayment showing the prominent beach-ridge sequence, Bulu River and floodplain, -and locations of the inner and outer embayments, and c) geomorphological sketch showing the location of GPR lines and samples for optical dating (see Table 2 for sample codes). The Vietnam (American) War bunker and the location of the artificial incision are also shown.

The northeast (winter) monsoon occurs from August to February and brings approximately 70% of the annual average rainfall between September to December, with average wind speed between 3.5 and 7 m/s from the north and northeast (Nghiem, 2009). The southwest (summer) monsoon is characterized by a dry period that spans from March to July with winds averaging between 3.5 and 4.5 m/s from the southeast (Nghiem, 2009).

The neap and spring tidal range for Danang (approximately 30 km southeast of Chan May and the closest accessible tide gauge data) ranges between 0.61 m and 0.72 m indicating a microtidal regime (Nghiem, 2009). Waves generally travel from an east-northeast direction and range in height from 1 to 3 m with periods of 8–10 s during the northeast monsoon, and southeast and north-northeast with heights ranging from 0 to 1 m and periods of 4–10 s during the remainder of the year (Do et al., 2018). Throughout the year, the waves strike the modern Chan May beach at an oblique angle as the waves are slightly refracted around the Chan May Peninsular in the east. A shore-normal transect from the mouth of the Bulu River recorded a water depth of 16 m approximately 4.5 km from shore (unpub. data).

Typhoons are commonly encountered in central Vietnam with 26 events passing within 100 km of Danang between 1982 and 2017, with 17 of these events making landfall (JTWC, 2019). Typhoons impacting central Vietnam commonly cause extensive damage to existing infrastructure (Wang et al., 2015). Notable typhoons that made landfall recently include Typhoon Xangsane in 2006 (maximum wind speed = 44 m/s and minimum pressure 940 hPa), Typhoon Ketsana in 2009 (maximum wind speed = 36 m/s and minimum pressure 960 hPa) and Typhoon Nari in 2013 (maximum wind speed = 39 m/s and minimum pressure

Table 1
Radar Facies observed in the GPR profiles from the GPR profiles collected from the Chan May embayment.

Radar facies	Image	Description	Location	Interpretation
1		Between two and three positive and negative couplets at the top of each profile	All profiles	The upper couplet is the air wave, second couplet is the groundwave and if the third couplet is present is due to imperfect placement of the transmitter and/or received on the ground surface (due to vegetation or uneven surface) generating an air-ground couplet
2	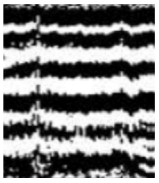	Multiple horizontal and parallel positive and negative couplets starting at the top of the profile and extending to depth	Where GPR passed over thick organic mud swales (e.g. Fig. 5)	This is ringing observed where the electromagnetic energy is bouncing between and within sedimentary units overprinting any stratigraphy
3	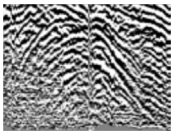	Large well defined hyperbolae superimposed or in isolation	Back of embayment or near roads (e.g. Fig. 2)	Where GPR has passed over large objects such as boulders or logs, or if in isolation is due to distant large metal objects (e.g. steel trucks) or transmission cables.
4		Long (many tens of metres), northward (towards the modern coast), shallow-dipping sequence of reflections ranging from 1° to 7°36′	Under all beach ridges from the back of the embayment to the modern shoreline (e.g. Fig. 4)	Prograding beachface facies showing the angle and orientation of the beachface at the time of deposition. The dips are apparent dips that closely resemble the true dip as profiles were close to perpendicular to the dip direction. Progrades dip in the direction of beach growth and are steepest at the back of the embayment and shallowest in the centre.
5	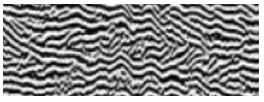	Short (up to 6 m long), southward (inland) dipping (0 to 4°) reflections located between two of Radar Facies 4 progrades	Only visible in 250 MHz antenna profiles and occurs along the lowest section of prograding beach facies (e.g. Fig. 4)	Landward dipping inclined surface reflecting swash bars that have migrated up the beach face within the swash zone. These surfaces become less steep and horizontal up the progrades. The uppermost swash bar occurs where there is a slight shallowing of the prograding beachface facies and marks the transition from swash zone to beachface. These likely formed after the readjustment of the offshore sediment budget after a storm erosional event.
6		Long convex upward reflections spanning 10's of metres in length	Visible throughout the profiles under abandoned and infilled channels (e.g. Fig. 3) or under the modern transgressive dune (e.g. Fig. 6)	Cross section of a river channel with relatively steep banks. The channel cross cuts other radar facies (i.e. Radar Facies 4) indicative of an erosional feature. Some channels range from 3 to 10 m deep and several tens of metres wide.
7		Trapezoidal packets with internal and upper flat horizontal reflections and parallel, steeply, inland dipping reflections.	Below transgressive dune (Fig. 6)	Storm surge fan with terminal foresets
8		Long flat, curved or shallowly dipping reflections coinciding with the terminations of overlying reflections	Throughout many of the profiles sequential sediment packages have built upon older sedimentary packages (e.g. Fig. 6)	Palaeo-surface marking the pre-transgressive and regressive Holocene land surface, or bounding surfaces between successive sediment packages (e.g. within or beneath the transgressive dune).
9	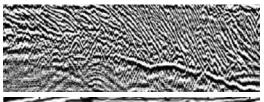	Shallow (3°) to steeply (14°) dipping sigmoidal reflections occasionally overlying Radar Facies 6 and dipping towards the centre of the channel	Only found along the meanders of the modern river (Fig. 9) and in a buried and infilled fluvial channel (see Fig. 3)	Epsilon cross beds as the river migrates and deepens laterally.
10	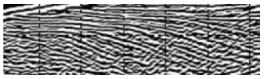	Horizontal parallel reflections transitioning to shallowly dipping inland and splayed reflections (10 to 15 m long) and steeply dipping (parallel to land surface) reflections	Only found within the transgressive dune (Fig. 7)	Formed by vertical and horizontal dune growth as sediment is accreted on top of the early dune and blown down the lee face.
11		Relatively flat or slightly dipping, long and discontinuous reflections with minor hyperbolae disrupting the reflections	Found at the back of the embayment and in near surface sediments elsewhere in the embayment (Fig. 2)	Undifferentiated sediments, located near the surface at the foot of the mountain where ground surface gradient changes from steep granitic mountain to flat coastal plain (i.e. scree), at the surface in swales and in dune sediments in 100 MHz profiles, and where swale sediments occur and ringing (RF2) does not obscure the GRP signal.
12	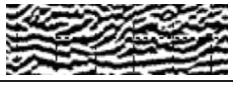	Concave-up reflections often disrupted by other concave reflections, with internal chaotic or dipping reflections	Found under the transgressive dune (Fig. 7)	Cross strata likely formed from dunes in a ridge and runnel system or back-beach tidal channel environment.

965 hPa) (Digital Typhoon, 2019). Earlier, Typhoon Bess in August 1968 and Typhoon Kate in October 1970 had similar measured minimum pressures (Digital Typhoon, 2019) attesting to the infrequency of moderate sized events.

4. Methods

Given the objectives of unravelling short-term versus longer-term coastal processes in Chan May, we collected GPR data and quartz OSL dating samples during three field campaigns in November 2011, May 2012 and January 2013.

4.1. GPR

Over 8.6 km of GPR data were collected from the Chan May embayment (Fig. 1) using the Sensors and Software® pulse EKKO GPR Pro with 100 and 250 MHz antennas. Profiles were collected along transects perpendicular to the modern coastline, with those from the northern part of the embayment collected from north to south, and those in the southwestern part of the embayment collected from northeast to southwest.

The 100 MHz GPR data were collected at 0.25 m increments while the 250 MHz GPR data were collected at 0.1 m increments. Both GPR systems were coupled with a real-time kinematic differential global positioning system (RTK dGPS) to accurately ascertain the local topography (horizontal error = 1.5 cm and vertical error = 4 cm). The dGPS heights and GPR profiles are tied to modern mean sea level through calibration with survey benchmarks located at significant engineering structures (e.g. bridges) throughout the Chan May embayment.

The GPR profiles were post-processed with Dewow, Automatic Gain Control (max. gain = 2000), migrated and the data topographically-corrected (Jol and Bristow, 2003; Neal, 2004). The electromagnetic velocity for topographic correction and migration were determined using the hyperbola velocity calibration in the EKKO Project v2 software. The velocity for most of the collected GPR profiles was 0.06 m/ns as the groundwater table was very close to the modern ground surface. The velocity through the transgressive dune was determined to be 0.12 m/ns, as the sediments were drier and the groundwater table was well below the ground surface. From the processed GPR profiles, radar facies (RF) that record similar electromagnetic characteristics are identified and were used for interpreting the subsurface stratigraphy.

4.2. Optical dating

Twelve quartz OSL samples were collected from strategic locations within the Chan May embayment (Fig. 1) to derive a chronology of

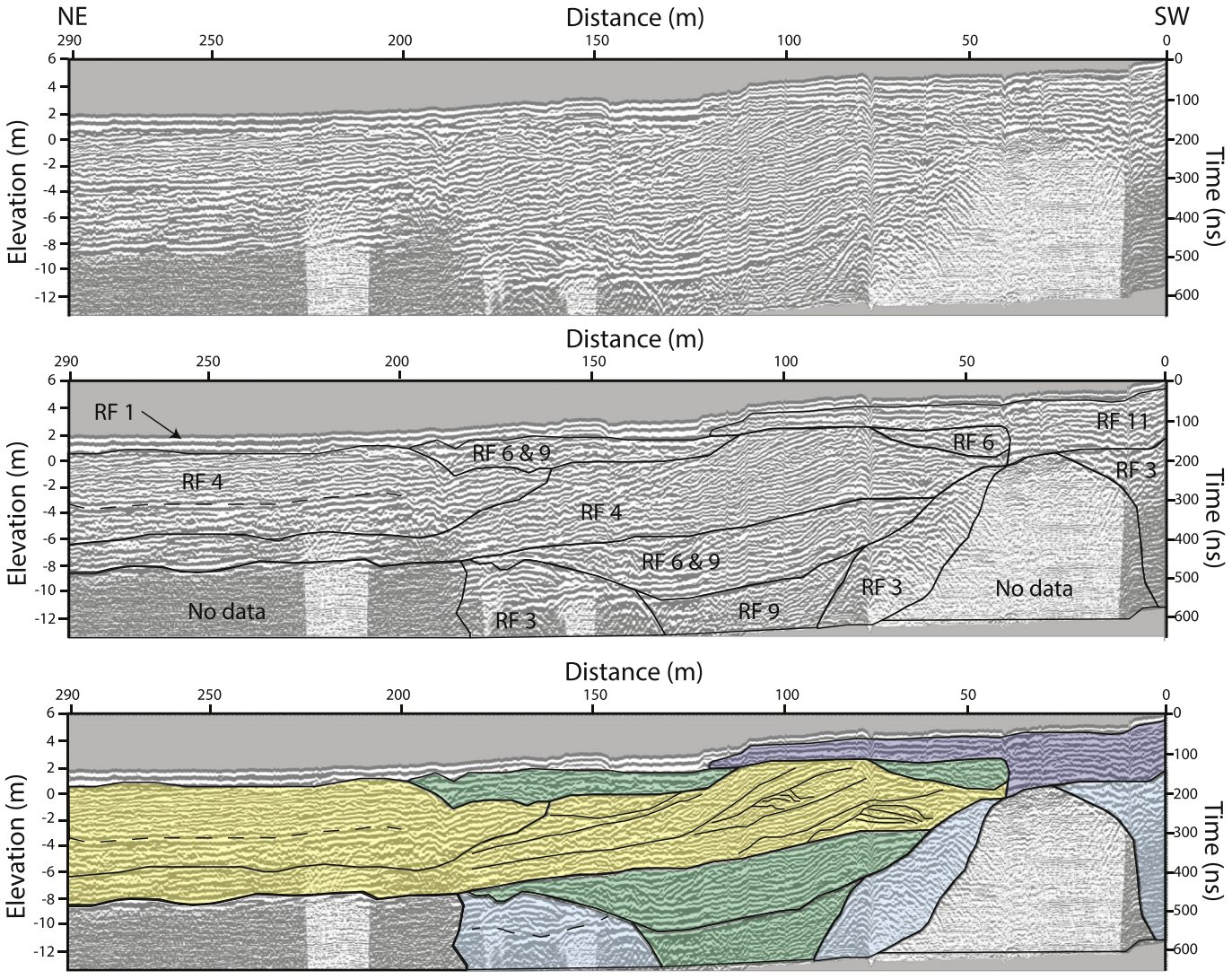

Fig. 2. 100 MHz GPR profile from the back of Chan May Embayment, a) processed GPR image, b) GPR image with interpreted radar facies (see Table 1), c) GPR image with the interpreted stratigraphy (purple = RF11 – undifferentiated scree deposits; light blue = RF3 – boulders; green = RF6 and RF9 – river channel and channel fill; yellow = RF4 – prograding beach ridges).

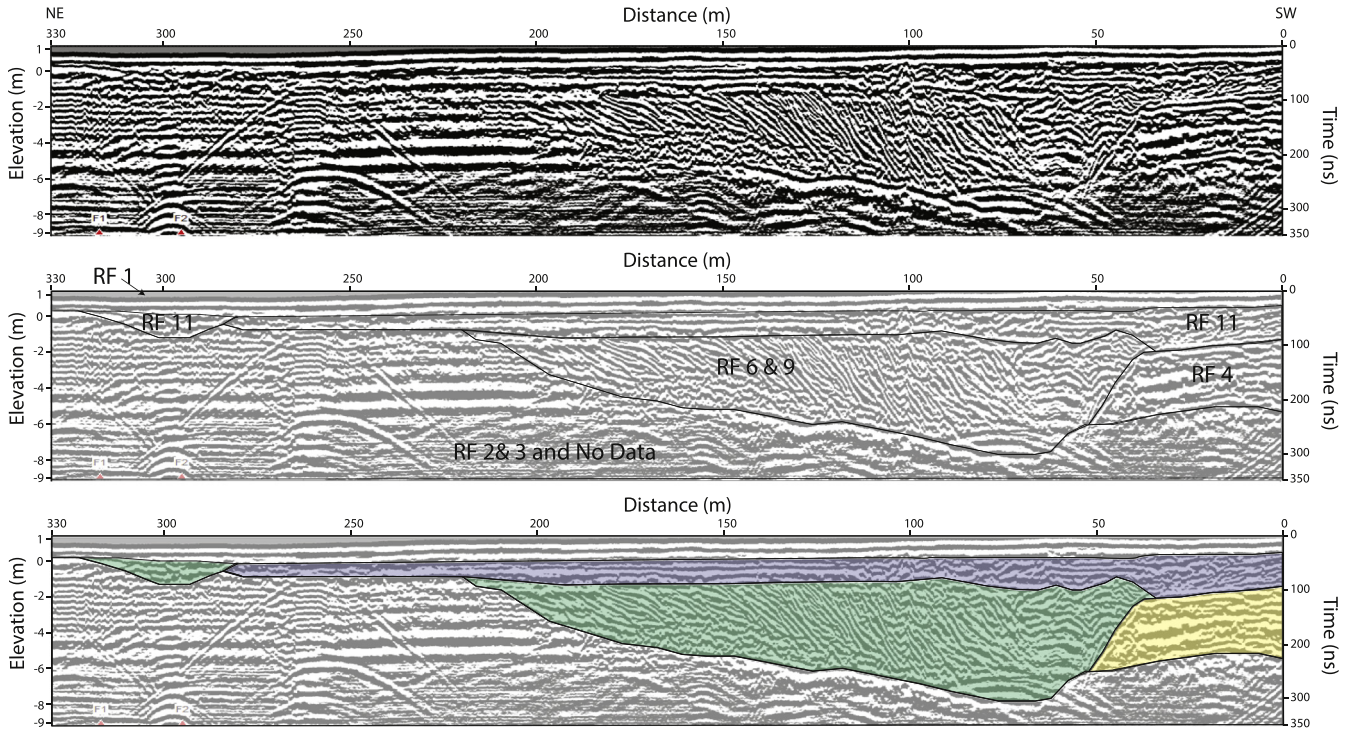

Fig. 3. 100 MHz GPR profile of the palaeoriver channel at the southern margin of the back of the Chan May Embayment, a) processed GPR image, b) GPR image with interpreted radar facies (see Table 1), c) GPR image with the interpreted stratigraphy (purple = RF11 – undifferentiated scree deposits; green = RF6 and RF9 – river channel and channel fill; yellow = RF4 – prograding beach ridges).

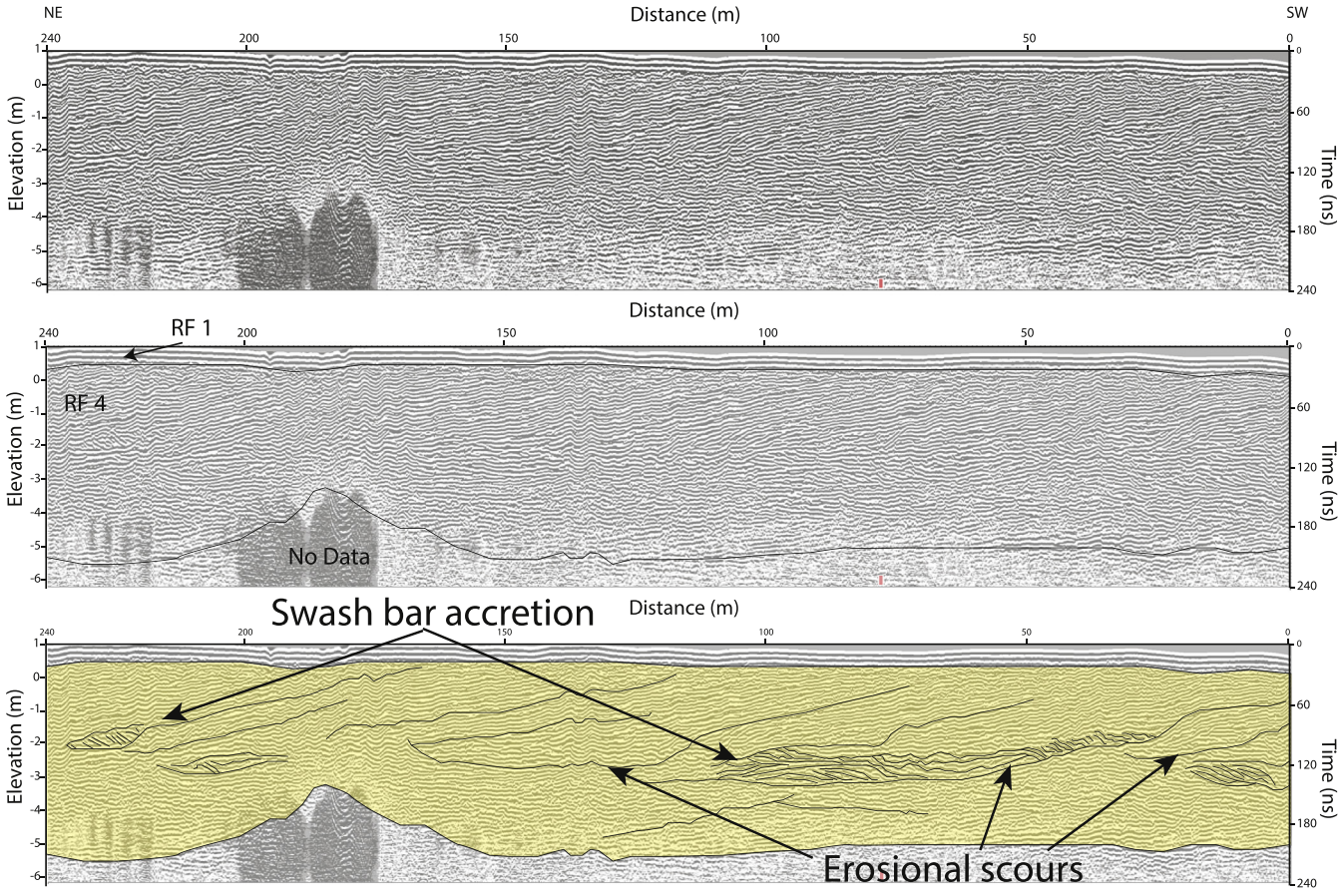

Fig. 4. 250 MHz GPR profile of the beach progrades near the back of the Chan May Embayment, a) processed GPR image, b) GPR image with interpreted radar facies (see Table 1), c) GPR image with the interpreted stratigraphy (yellow = RF4 – prograding beach ridges with erosional scours and swash bar accretion).

the evolution of the embayment. The identification of quartz OSL targets was determined following examination of the GPR profiles and geomorphology of the embayment. Samples were then collected from the back of the embayment (NP1, NP2), from 3.4 km from the modern coast (LV1, LV2), from the large scroll bar system (OSL1, OSL2, OSL3, OSL4), from the beach ridges preserved at T1F2 (BR1, BR2, BR7), and from an inferred overwash deposit (CD1) beneath the modern transgressive dune ca. 450 m from the modern coastline.

Quartz OSL samples were collected by hammering 30 cm long, 5 cm diameter, light-tight PVC pipes into the sediment after either augering down to the required depth or from trench faces dug into the sediment (e.g. T1F2). The plastic tubes were then capped, placed in black plastic bags and transported to the Luminescence Dating Laboratory of the University of Liverpool.

Samples were prepared using standard quartz OSL techniques: sieving to 90–150 μm, 125–150 μm or 150–200 μm fractions, treating with HCl and H_2O_2 and extracting the quartz grains using heavy liquids at 2.62 specific gravity (s.g.) and 2.76 s.g. The clastic component was then treated with 40% HF for 40 min, and the samples sieved again using 90 μm, 100 μm or 125 μm. All measurements were conducted on 3 mm aliquots and initial tests concerning thermal treatment and laboratory beta doses revealed intrinsically bright quartz grains for all samples. The standard single aliquot protocol with a preheat of 260 °C/10 s could therefore be employed for all samples except for the scroll bar samples (OSL1, OSL2, OSL3, OSL4) for which a lower preheat temperature was used (240 °C). For data analysis, standard rejection criteria were used resulting in an average aliquot acceptance rate of 70–90%. The dose rate of each sample was determined by first recording a gamma spectrum followed by converting the resulting activities of uranium, thorium and potassium into annual dose using standard conversion factors (Guérin et al., 2011). Although radionuclide content varies enormously, the ages of all samples presented here are in stratigraphic order.

5. Results

5.1. Radar facies

From the GPR profiles, we recognize 12 distinct GPR facies (RF) that we ascribe to either variations in the electromagnetic interaction with the sediments or to sedimentary facies (Table 1). RF are commonly located in close proximity and can be grouped as radar facies associations. For example, RF 3 (buried objects, e.g. boulders), RF 6 (basal channel scour) and RF 9 (epsilon cross beds) occur together as relict river channels with the basal scour, occasionally overlain by a thin bed of boulders and in turn overlain by epsilon cross beds that dip and steepen towards the thalweg recording the morphology of the point bar on the inside of the channel bend as the river channel migrated laterally. From the thalweg to the opposite river bank, epsilon cross beds do not form and the channel is infilled with coarse debris.

5.2. Radar profiles

Figs. 2–8 show seven selected GPR profiles representing different surface and subsurface features within the Chan May embayment ordered with respect to distance from the modern coast. Fig. 9 profiles the scroll bars in the Bulu River.

From the back of the Chan May embayment, at the foot of the Truong Son Range, the GPR profile (Fig. 2) records a complex array of different radar facies, including RF 3, 4, 6, 9 and 11 that record lateral and vertical variation in radar stratigraphy. In the landward part of the GPR profile, data are attenuated approximately 6 m below the land surface, but adjacent hyperbolic reflections occur (RF 3), which in turn are overlain by convex upwards reflections (RF 6) and horizontal discontinuous reflections (RF 11). At approximately 50 m from the start of the GPR profile long, continuous, steeply-dipping (up to 6°) reflections (RF 4) onlap RF 3, and overlie complex convex-upward reflections (RF 6) with

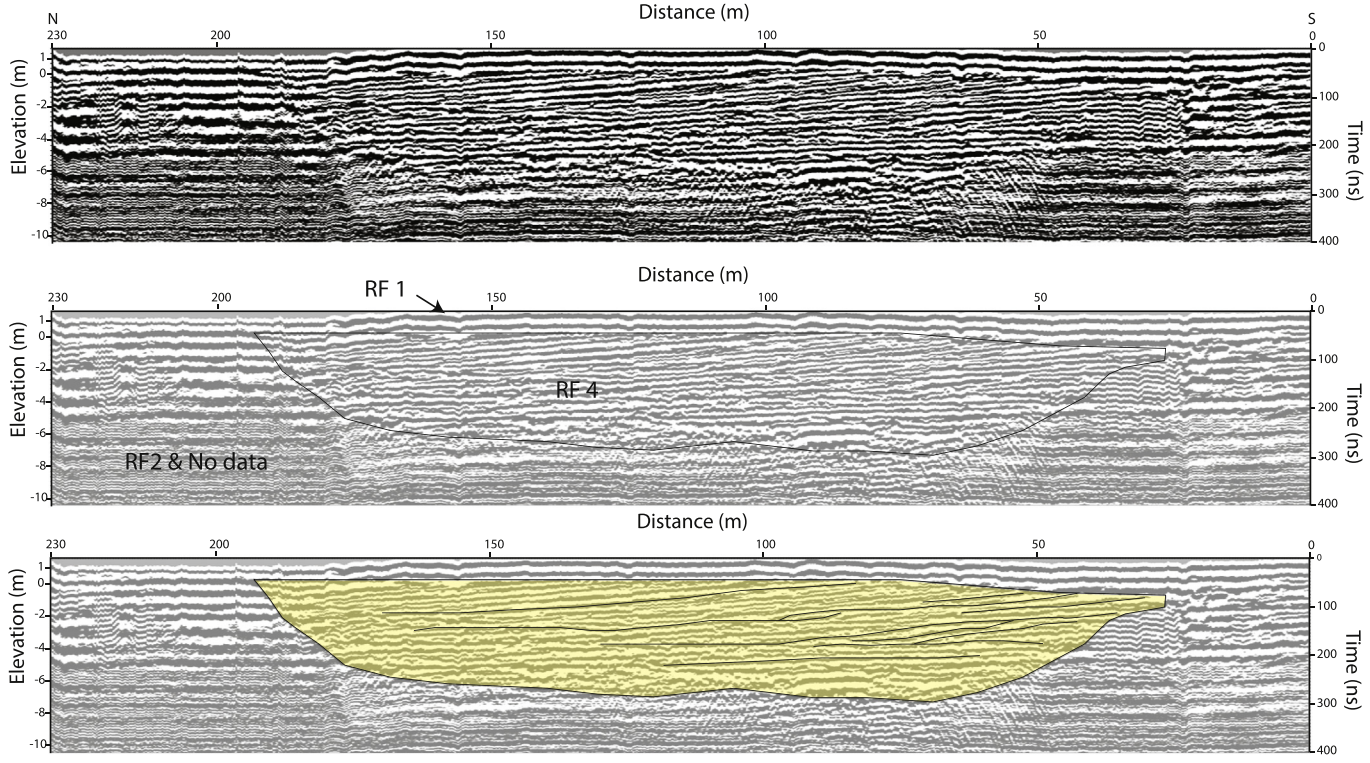

Fig. 5. 100 MHz GPR profile of the beach progrades in the east of the Chan May Embayment a) processed GPR image, b) GPR image with interpreted radar facies (see Table 1), c) GPR image with the interpreted stratigraphy (yellow = RF4 – prograding beach ridges. Note that erosional scours and swash bar accretion are not observed in this radar facies).

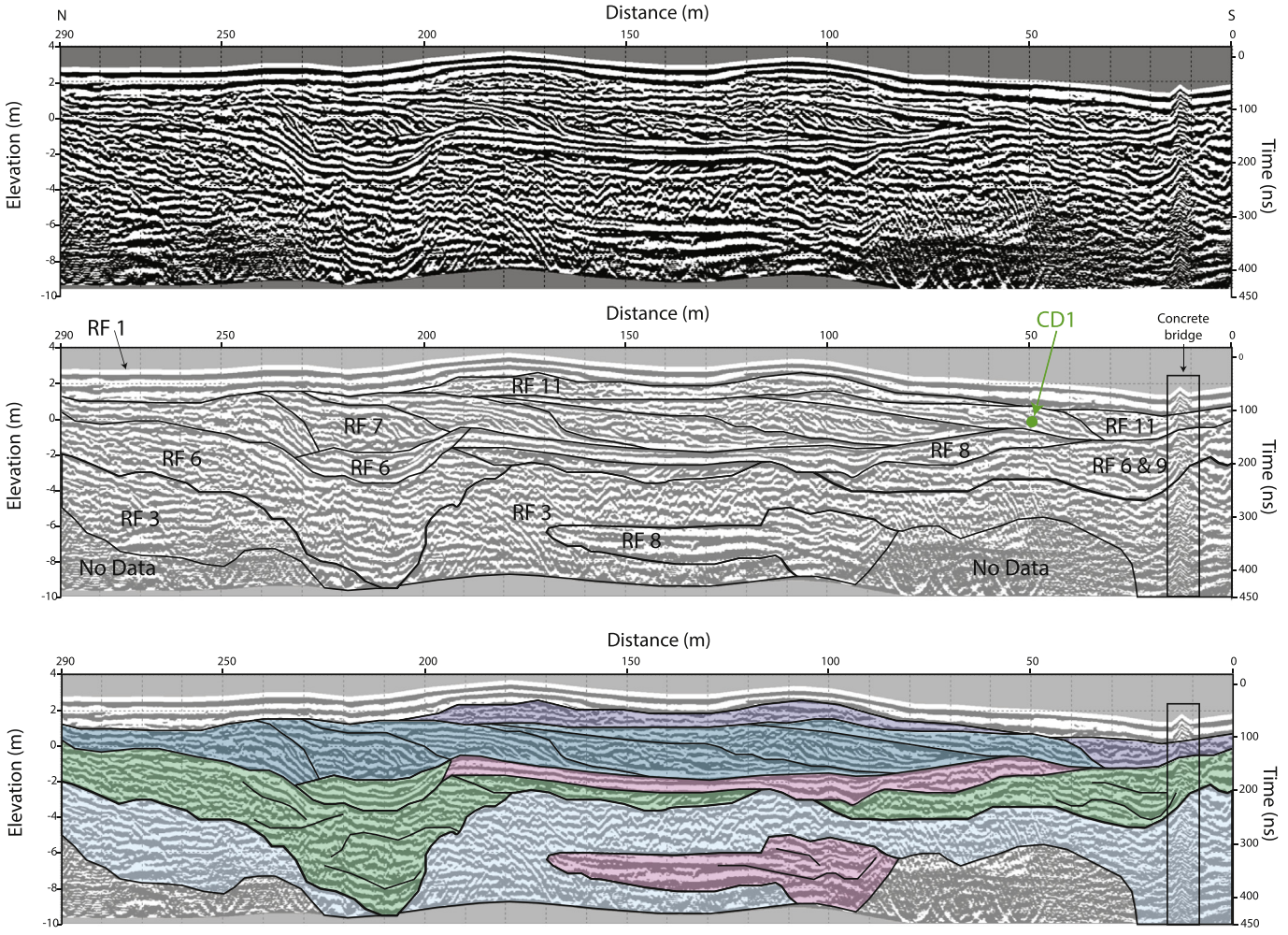

Fig. 6. 100 MHz GPR profile of the transgressive dune near Canh Duong village in the north west of the Chan May Embayment, a) processed GPR image, b) GPR image with interpreted radar facies (see Table 1), c) GPR image with the interpreted stratigraphy (purple = RF11 – undifferentiated scree deposits; green = RF6 and RF9 – river channel and channel fill; pink = RF8 – distinct bounding surface reflecting a palaeosurface; deep blue = RF7 – washover fans). Green dot shows the location of the sample CD1.

weakly sigmoid-shaped reflections dipping into the depression (RF 9). The upper steeply dipping reflections at 50 to 150 m along the profile shallow to sub-horizontal reflections as the reflections overlie a zone of no GPR data from ca. 180 to 290 m along the profile. Directly overlying these horizontal reflections is another sequence of very shallowly dipping reflections (RF 4).

Fig. 3 extends across a series of rice paddies that have been developed above a 7 m deep and ca. 200 m wide asymmetric, concave upward reflection (RF 6) containing shallow to steeply dipping sigmoidal reflections. This radar facies association truncates shallow dipping long continuous reflections (RF 4) to the southwest.

The remainder of the embayment is dominated by long and continuous, low-angle (ca. 1°), inclined reflections that dip towards the sea (RF 4; e.g. Figs. 4 and 5). Compared with the 100 MHz antenna profiles (Fig. 5), the 250 MHz antenna profile (Fig. 4) shows significantly more internal structure with long continuous reflections also dipping shallowly towards the coast. As depth in the 250 MHz profiles increases, the reflections flatten and frequently display a convex upward shape. Within these concave upward reflections are distinct climbing, landward dipping reflections (Fig. 4).

Near the modern coastline, Fig. 6 records either no data, or many hyperbolic reflections (RF3) in the lower sections of the profile. Within, directly overlying or truncating this facies are several packages of convex upwards reflections (RF 6) that grade laterally to or are overlain by long, horizontal reflections (RF 8). Above RF 8 are six landward dipping trapezoidal units (RF 7) that downlap onto the underlying units. The landward contact is sigmoidal. Overlying these trapezoidal units is a thin facies of unstructured reflections (RF 11) and landward of the trapezoidal units is organic-rich, water-logged sediment within the swale.

Fig. 7 shows a 250 MHz antenna profile over the currently active, transgressive dune. Within the transgressive dune, inland dipping reflections build upward and occasionally diverge inland (RF 10). The inland dipping reflections parallel the lee dune face. Beneath the stoss face of the transgressive dune are two packets of a series of four metre wide and one metre deep concave reflections (RF 12) that are similar to RF 5 but lack the distinctive landward dipping internal reflections. Separating these packets is a distinct bounding surface. Similar, but large concave reflections (8 m long by 2 m deep) also occur below the lee side of the modern transgressive dune. Coastward of the stoss side of the transgressive dune, long reflections dip towards the coast away from the dune (RF 4), representing the re-initiation of beach progrades.

A 250 MHz antenna profile extending from the modern beach inland (Fig. 8) records elongate, shallow, northward–dipping reflections (RF 4). Fig. 9 shows a profile across the scroll bars (RF 9) formed at the major bend in the Bulu River, which show reflections with a very shallow dip to the southwest. In plan view (Fig. 1), the scroll bars have distinct ridges that the GPR records as discontinuous reflections (RF 11).

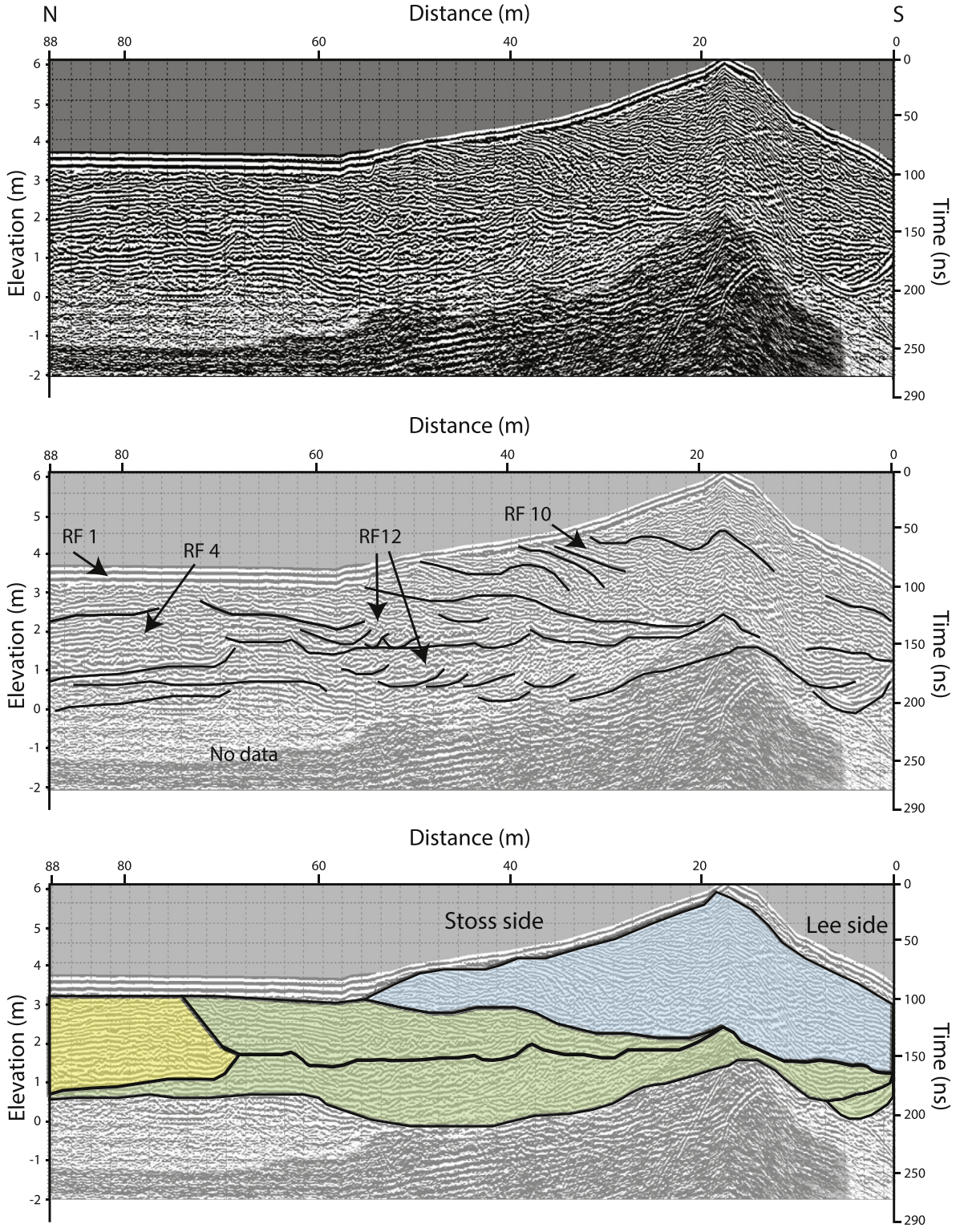

Fig. 7. 100 MHz GPR profile of the transgressive dune behind the sand mined region (Lee et al., 2012, 2013) in the north of the Chan May Embayment, a) processed GPR image, b) GPR image with interpreted radar facies (see Table 1), c) GPR image with the interpreted stratigraphy (green = RF12– small superimposed channels; yellow = RF4 – prograding beach ridges; pale blue = RF10 – transgressive dune facies).

5.3. Optical dating

Table 2 shows the results of the OSL analyses and Fig. 10 shows these results on a map of the Chan May embayment. The oldest age was recovered from the exposed beach ridge from the back of the embayment and is dated at 6.3 ± 0.2 ka (NP2) and all subsequent dates become younger towards the modern beach. Date NP1 is considered too young as it was collected from a disturbed part of the relict foredune. The two ages obtained from Loc Vinh (LV1 and LV2) come from different depths, but are both within error and give a mean age of 3.7 ± 0.4 ka.

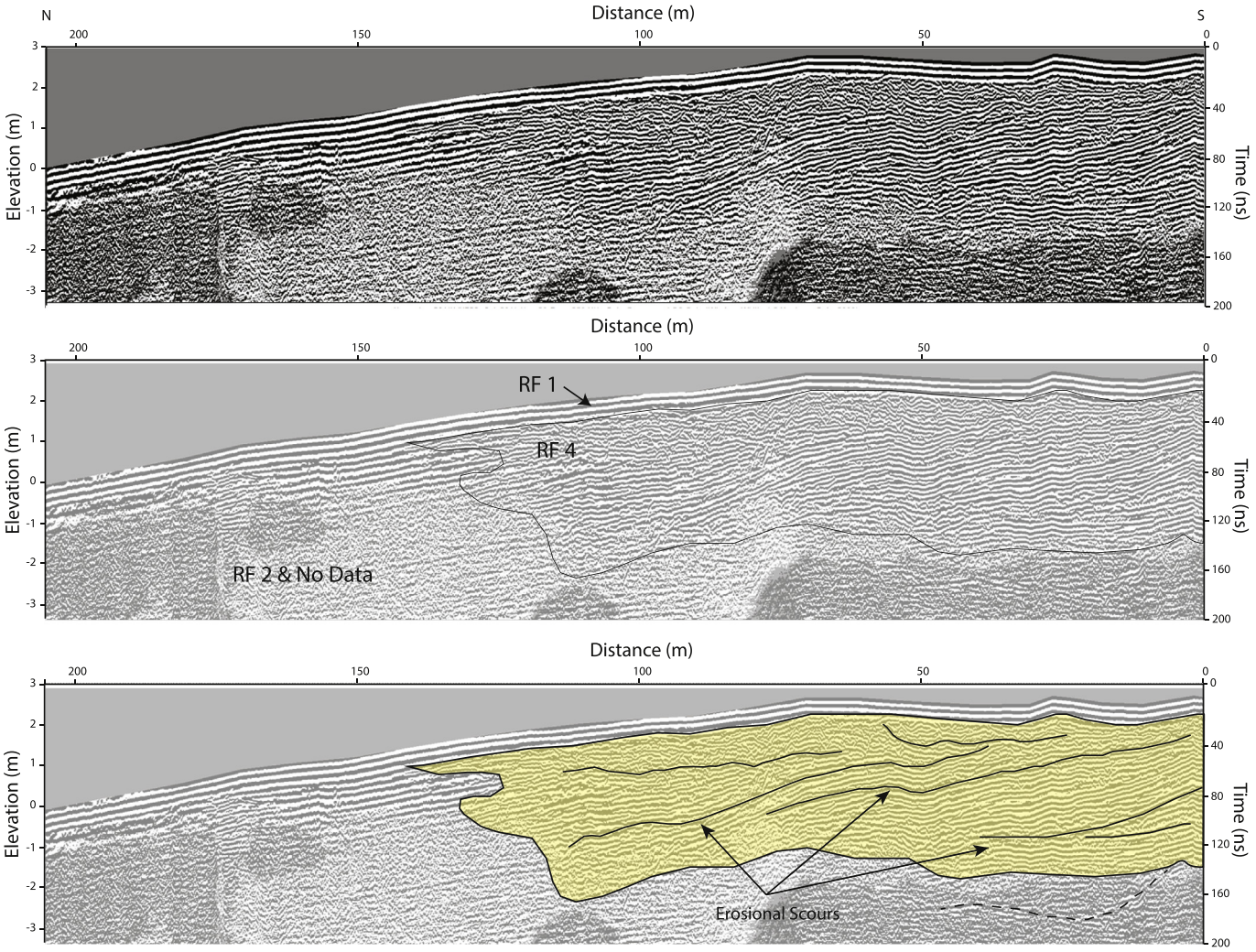

Fig. 8. 100 MHz GPR profile of the beach progrades transitioning to the modern beach in the northwest of the Chan May Embayment, a) processed GPR image, b) GPR image with interpreted radar facies (see Table 1), c) GPR image with the interpreted stratigraphy (yellow = RF4 – prograding beach ridges).

The three ages obtained from T1F2 along the Bulu River record an older date in the sands from the prograding beach deposits (BR1–2.6 ± 0.3 ka) and two overlapping dates at BR2 (2.0 ± 0.2 ka) and BR7 (1.9 ± 0.2 ka) giving a mean age of 1.9 ± 0.3 ka. BR 2 and BR7 are separated by ~1.7 m suggesting rapid vertical accretion of the sediments during this period. The BR7 sample contains a much higher U concentration, possibly due to a different sediment source supplying sand to the region.

Four quartz OSL ages from the scroll bars were obtained, with OSL1 (1.9 ± 0.2 ka) and OSL2 (2.0 ± 0.1 ka) collected 65 m apart from the same depth on the same scroll bar, and OSL3 (1.6 ± 0.1 ka) and OSL4 (1.9 ± 0.2 ka) collected 70 m apart from the same depth from the innermost scroll bar. All four ages overlap (at 2 sigma) indicating that the 520 m of sediments that separates the innermost (OSL3 and OSL4) and centrally-located (OSL1 and OSL2) scroll bars were deposited very rapidly at ca. 1.84 ± 0.3 ka. Unfortunately, the scroll bars situated on the modern bank of the Bulu River (ca. 1150 m from OSL1 and OSL2) were inundated at the time of fieldwork and could not be accessed for dating to establish if the scroll bars have continued to form to the present day or if there has been a hiatus in their formation.

A single quartz OSL date (CD1) from the most inland trapezoidal radar packet (RF 7) preserved beneath the transgressive dune recorded a modern age. As this radar packet predates the formation of the transgressive dune, the transgressive dune is here considered to have formed recently.

6. Interpretation of the coastal evolution of the Chan May embayment

The contact between the Truong Son Range and the more recent sediments examined through GPR analysis shows a complex margin with zones of no data inferred to be granitic bedrock and accumulations of buried boulders that may have been eroded from the granitic bedrock or that the bedrock had been deeply incised and filled (RF 3, Fig. 2). Overlying these boulders is a remnant of a small channel (RF 6) that abuts and is overlain by undifferentiated sediments (RF 11) that is here interpreted as surficial scree sediments derived from the higher slopes (Fig. 2). The small channel and scree deposits overlie, partially erode and obscure the first undated beach ridge (RF 4) in the Chan May Embayment. This first beach ridge sequence onlaps the boulder deposits, and overlies two buried palaeochannels (RF6 and RF9) in the southwest (Fig. 2).

The most common GPR reflection from the sediments within the embayment are long, continuous shallowly-dipping (1.0–3.5°) reflections constituting RF 4 interpreted as beach, foreshore and upper shoreface deposits recording the progradation of the beach from ca. 6.2 ka as the embayment has been filled (Figs. 3–8). This interpretation is reinforced by the 250 MHz GPR profile extending inland from the modern high tide mark (Fig. 8). The dipping reflections (ca. 1°) parallel the modern beachface and extend inland to the back of the embayment and show very little variation in dip (e.g. Figs. 4 and 5). Within the beach

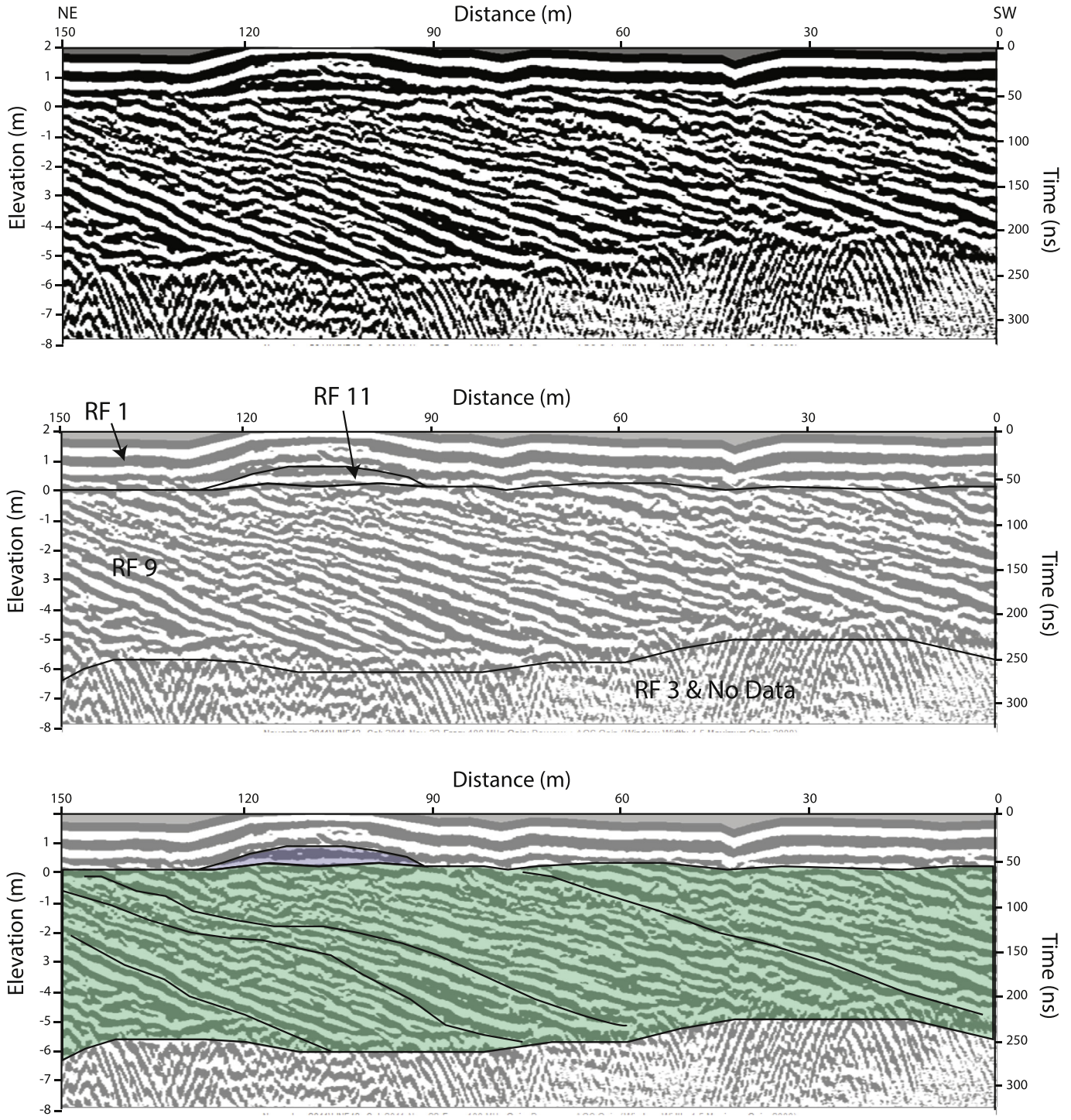

Fig. 9. 100 MHz GPR profile of the large scroll bar system associated with the Bulu River. This section is representative of the scroll bar system, and occurs between the scroll bars from which the quartz OSL samples were collected (see Fig. 1), a) processed GPR image, b) GPR image with interpreted radar facies (see Table 1), c) GPR image with the interpreted stratigraphy (purple = RF11 – aeolian reworked; green = RF9 – epsilon cross beds. Note that channel base (RF6) is not observed in this image).

ridge system are packets of erosional scours as the beach has been locally eroded, and a series of mounds indicative of longshore bars, and suggestive of landward migration of swash bars within the palaeo-swash zone (e.g. Fig. 4). We infer that swash bar accretion has replenished the sediments on the beach face before returning to beach prograding facies (Figs. 4 and 8). The radar facies and environmental interpretation invoked for the progradation mechanism of the Chan May beach ridge section is similar to the interpretations of other coastal sites around the world (e.g. Bristow et al., 2000; Bristow and Pucillo, 2006; Tamura et al., 2008; Clemmensen and Nielsen, 2010; Hein et al., 2013; Mallinson et al., 2014). Between successive beach ridges, the electromagnetic signal does not penetrate the organic muddy swales as recorded by the extensive ringing in the muddy units (RF 2) that differs to the swale at the back of the embayment (e.g. Fig. 5).

The exposed section of beach ridges throughout the Chan May embayment are slightly elevated above the topographically lower swales (<50 cm) and these raised sections are composed of reworked aeolian sands forming relict foredunes (Shepherd, 1991).

A palaeo-fluvial channel is also observed (Fig. 3) and consists of a basal scour (RF 6), and epsilon cross beds (RF 9) as the channel migrated

Table 2
Analytical data obtained for optical dating and resulting ages. Sediment depth indicates either the exact depth below surface for horizontally collected samples or the depth range for samples collected vertically. Water content is deduced from field moisture and error margin includes dryness or saturation level. Effective dose rate (dose $rate_{eff}$) is derived from radionuclide content converted to the sum of beta and gamma dose rates (Guerin et al., 2011) including absorption of water and contribution from cosmic radiation.

Sample ID	Location	Lat	Long	Sediment depth (cm) below surface	Approx. distance from modern coastline (m)	Grain size (μm)	Water content (%)	U (μg g^{-1})	Th (μg g^{-1})	K (wt %)	D_e (median; Gy)	Dose $rate_{eff}$ (Gy/ka)	OSL age (±1σ, a)
CD1	Canh Duong	16°18′ 38.93″N	107°58′ 58.21″E	131–161	615	90–150	20 ± 5	4.4 ± 0.1	15.55 ± 0.27	0.23 ± 0.01	–	1.97 ± 0.07	modern
OSL1	Scroll bars	16°17′ 28.32″N	107°57′ 31.20″E	60	3700	90–150	2 ± 2	1.70 ± 0.04	5.19 ± 0.12	0.56 ± 0.02	2.8 ± 0.3	1.34 ± 0.02	1910 ± 210
OSL2	Scroll bars	16°17′ 26.76″N	107°57′ 32.70″E	60	3700	90–150	2 ± 2	1.77 ± 0.05	4.98 ± 0.11	0.41 ± 0.01	2.6 ± 0.2	1.20 ± 0.01	1970 ± 150
OSL3	Scroll bars	16°17′ 41.94″N	107°57′ 40.56″E	44	3300	90–150	14 ± 2	2.09 ± 0.05	6.81 ± 0.14	0.81 ± 0.02	2.7 ± 0.2	1.58 ± 0.03	1580 ± 120
OSL4	Scroll bars	16°17′ 40.20″N	107°57′ 42.00″E	44	3300	90–150	14 ± 2	2.44 ± 0.06	7.95 ± 0.16	0.74 ± 0.02	3.4 ± 0.3	1.66 ± 0.03	1900 ± 170
BR7	Bulu River	16°18′ 20.97″N	107°58′ 44.40″E	60	1240	90–150	2 ± 2	8.32 ± 0.19	30.15 ± 0.48	0.17 ± 0.01	8.3 ± 0.7	4.26 ± 0.22	1890 ± 180
BR2	Bulu River	16°18′ 20.97″N	107°58′ 44.40″E	230	1240	125–150	20 ± 5	1.07 ± 0.03	2.95 ± 0.08	0.39 ± 0.01	2.1 ± 0.2	0.82 ± 0.01	2000 ± 190
BR1	Bulu River	16°18′ 20.97″N	107°58′ 44.40″E	255	1240	125–150	20 ± 5	1.14 ± 0.03	3.66 ± 0.09	0.66 ± 0.02	2.7 ± 0.3	1.08 ± 0.02	2570 ± 290
LV1	Loc Vinh	16°16′ 56.97″N	108° 0′ 59.33″E	153–120	3600	100–150	20 ± 5	0.76 ± 0.02	1.86 ± 0.07	0.24 ± 0.01	2.1 ± 0.2	0.478 ± 0.004	3610 ± 350
LV2	Loc Vinh	16°16′ 56.97″N	108° 0′ 59.33″E	43	3600	100–150	20 ± 5	0.65 ± 0.02	1.11 ± 0.07	0.26 ± 0.01	2.2 ± 0.1	0.601 ± 0.009	3840 ± 180
NP1	Nam Phuoc Riverbank	16°15′ 35.11″N	107°55′ 26.01″E	90	10,000	90–150	18 ± 2	0.45 ± 0.02	2.04 ± 0.07	0.46 ± 0.01	3.9 ± 0.8	0.769 ± 0.008	5070 ± 160
NP2	Nam Phuoc Riverbank	16°15′ 35.11″N	107°55′ 26.01″E	85–116	10,000	90–150	30 ± 3	0.46 ± 0.02	1.59 ± 0.07	0.36 ± 0.01	3.8 ± 0.1	0.600 ± 0.007	6290 ± 230

and deepened to the southwest and was eventually infilled, which likely occurred when the Bulu River was redirected out of the main channel. The development of this fluvial channel post-dates the formation of the beach ridge sequence here as the fluvial facies truncate the beach ridge facies (RF 4) to the southwest (Fig. 3).

The modern transgressive dune contains and buries complex geomorphic features. In the 100 MHz profile (Fig. 6) are a series of fluvial channels consisting of RF 6 and 9, which are in turn overlain by six trapezoidal units (RF11) indicative of the terminal foresets of storm washover fans. Nearby, the 250 MHz antenna profile (Fig. 7) preserves RF 10, represents the constructional phase of the transgressive dune where sediment is blown inland begins to build upward and sand topples down the lee face building the dune inland, i.e. dune roll over. The concave upward features (RF 12) in

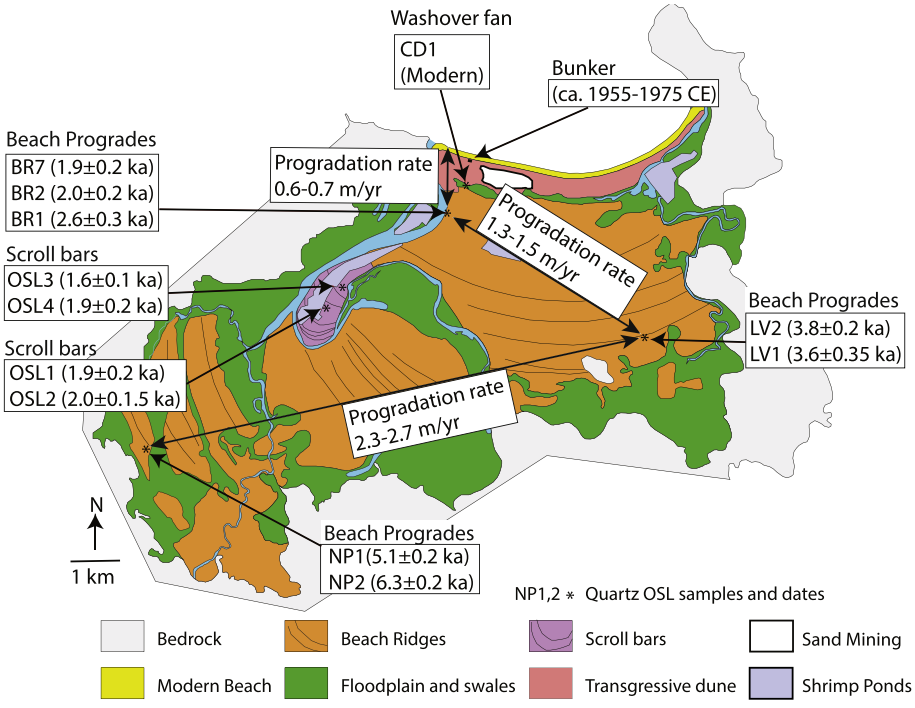

Fig. 10. Map of the Chan May embayment showing the sites and ages of the quartz OSL samples, the calculated progradation rates between successively dated portions of the coastline, and the location of the Vietnam (American) War bunker.

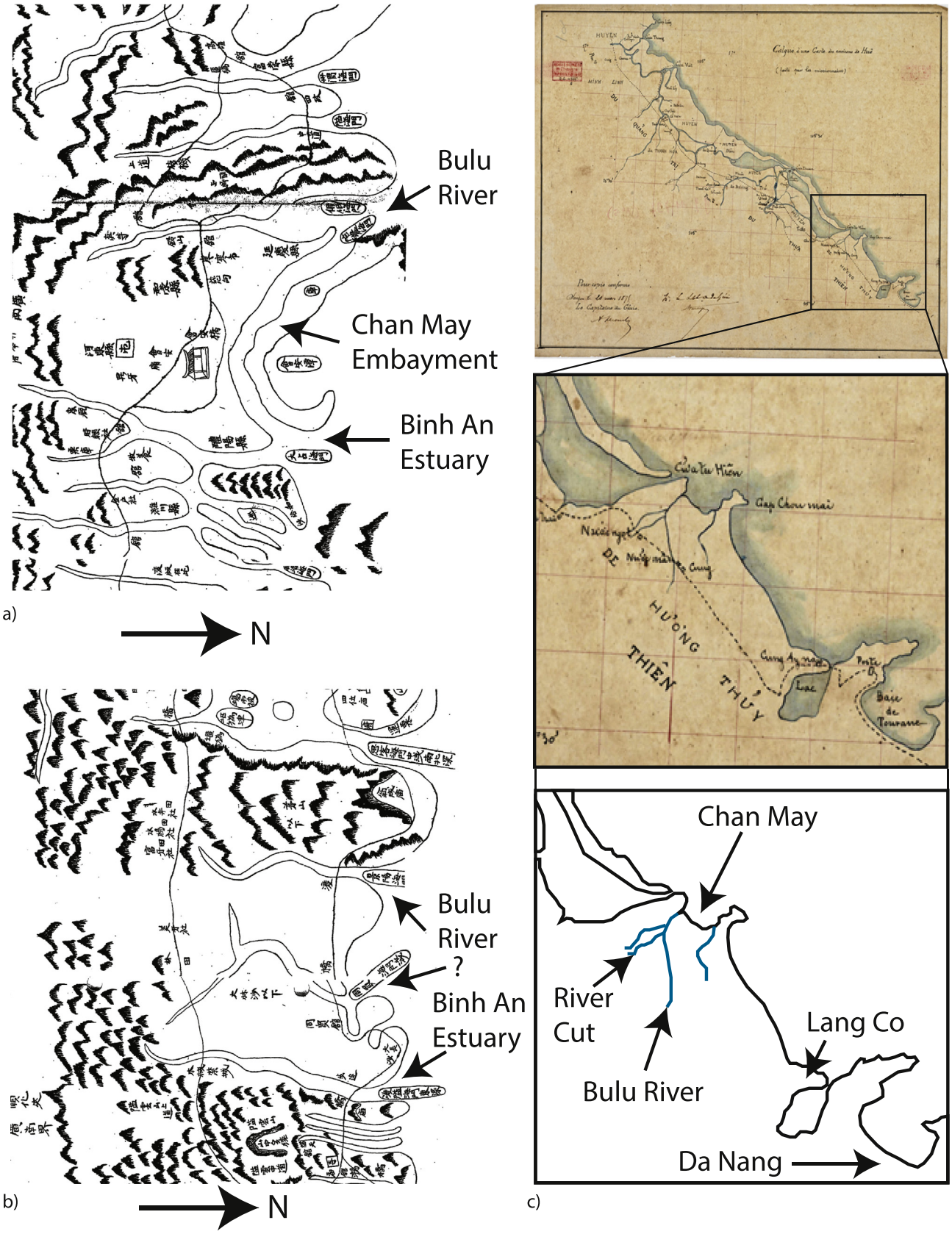

Fig. 11. Historical maps of Chan May embayment, a) 1630–1655 map of the Chan May embayment showing the Bulu River hugging the western side of the embayment. In this map, the Bulu River opens to the east and west of the embayment and feeds the Binh An Estuary via the modern day swale behind the transgressive dune. b) 1655–1690 map suggesting that the connection of the Bulu River to the Binh An Estuary had ceased. The forking river channel in the centre may be the abandoned northward flowing channel in the centre of the Chan May Embayment (see Fig. 1). c) 1875 French map showing the Bulu River having three points of confluence near the modern day scroll bars (Pacha Hum-an Project, 2019). a) and b) are modified from Schweyer (2016).

Fig. 7, likely are sets of trough cross-bedding from 3 dimensional dune migration with the flow directed perpendicular to the GPR profile, and could be from either dunes in a ridge and runnel beach system or a back-beach tidal channel with water flowing parallel to the coastline. Of note, beneath the transgressive dune in this profile are no obvious radar facies that represent the prograding beachface common in all other profiles, but these start seaward of RF 12 in Fig. 7.

The scroll bars on the modern Bulu River preserve typical epsilon cross bed features (RF 9) showing that sediment has accreted on the inner bank of the meander as the Bulu River eroded and migrated through the beach ridge strandplain (Figs. 1 and 9).

7. Discussion

7.1. Initiation of the beach-ridge plain sedimentation

The contact between the beach ridge sands and underlying boulder, fluvial and bedrock units (Fig. 2) is inferred to be the land surface demarcating the contact between an exposed terrestrial surface that was rapidly flooded during the mid-Holocene sea-level highstand (e.g. Ta et al., 2002), and the overlying beach ridges, which formed during later shoreline regression. Although we were unable to directly date these initial beach ridge sands, a quartz OSL date of 6.3 ± 0.2 ka from 116 to 85 cm below the modern ground surface and located within the exposed back-most beach ridge in the embayment (NP2) supports the interpretation that the entire beach ridge sequence formed after the mid-Holocene sea-level highstand. The buried initial beach ridge foreshore clinoforms show steeper dips (6°) than those recorded elsewhere in the embayment due to the onlapping of these strata onto granitic basement. The truncated upper surface of this beach-ridge facies occurs at ca. 2.3 m above pmsl. Our ca. 2.3 m above pmsl observation of the upper beach ridges may be in response to this dip, or a lower sea level highstand (Ta et al., 2002) or date from a time after the maximum highstand.

7.2. Beach ridge progradation rates

The mean progradation rate from the second oldest beach ridge to modern coastline ranges from 1.54 to 1.66 m/yr (oldest age divided by the distance to the modern shoreline); however, some variation in progradation rate appears to occur with the rate of progradation decreasing towards the coast since the mid-Holocene sea level highstand. From 6.3 ± 0.2 to 3.7 ± 0.4 ka (NP to LV), the coastline prograded on average 2.–2.7 m/yr; from 3.7 ± 0.49 to 1.9 ± 0.3 ka (LV to BR2 and BR7), the coastline prograded on average 1.3–1.5 m/yr and from 1.9 ± 0.3 ka to the present (BR2 to modern coastline), the beach prograded on average 0.6–0.7 m/yr (Fig. 10).

Historical maps of the region (Fig. 11a–c; Schweyer, 2016; www.pascha.hum-an.org) show that beach progradation occurred between 1630 and 1655 (Fig. 11a) and 1875 (Fig. 11c), and that progradation continued until recently (Figs. 1 and 6). In addition, there is no field evidence to suggest that the modern shoreline is being eroded, and with vegetated (up to ca. 25 m high mature *Casuarina* sp. trees) intact berm and back-beach environment. Although *Casuarina* trees can grow very rapidly in sandy, nutrient poor high-salt content sediments, the vegetated back-beach also contain concrete bunkers that housed military anti-aircraft and anti-beaching armed forces that were used during the Vietnam (American) War (Fig. 1). These concrete bunkers are located 2 m landward of the edge of the vegetated berm. This suggests that the modern beach is in the same location as it was between ca. 1955 and 1975. More recent maps of the Chan May embayment do not show that the beach extended beyond the 1955–1975 and today's position. Consequently, it is reasonable to conclude that coastal progradation occurred until at least the 1955–1975 period.

The progradation rates calculated here are long term averages and we do not attempt to consider punctuated erosional events (e.g. storms of varying magnitude) and higher rates during beach rebuilding phases (e.g. Buynevich et al., 2007, 2011; Cunningham et al., 2011; Tamura et al., 2019b) inferred from the swash bar migration and merging with prograding beach facies. In addition, quartz OSL samples were not collected from obvious breaks where pre-existing beach facies were eroded and subsequently rebuilt (e.g. Bristow and Pucillo, 2006; Tamura et al., 2019b) and thus actual progradation rates may vary.

Progradation rates have been shown to vary in numerous locations and have been ascribed to several mechanisms. Bristow and Pucillo (2006) suggested a four-fold decrease in progradation rate from older to younger sediments in Guichen Bay, South Australia. Bristow and Pucillo (2006) ascribe this decrease in progradation rate to changes in wind and wave climate and increase in the offshore accommodation space. Sloss et al. (2018) determined declining progradation rates of 3 m/yr and 1.67 m/yr during the sea-level regression after the Holocene sea-level highstand in the Gulf of Carpentaria, northern Australia. The most recent coastal progradation at this site has been ascribed to intensification of El Niño since ca. 1900 years ago (Sloss et al., 2018). At Pedro Beach in southeastern Australia, Oliver et al. (2019) identified a decrease in coastal progradation rate from ca. 7 to 3.9 ka, and termination of coastal progradation at ca. 3.9 ka. Oliver et al. (2019) ascribe this termination of progradation to a decline in the accommodation space as the prograding beaches reached the oceanward limit of the marginal headlands and excess sediment was mobilized out of the adjacent coastal zone via longshore currents to other beaches. Sharples et al. (2020) examining historical records of Ocean Beach, western Tasmania, identified a potential tipping point from an episodically eroded prograding beach system to persistent coastal recession following a storm or series of storms and in conjunction with recent sea level rise.

Elsewhere in Southeast Asia, coastal progradation rates of 1–1.8 m/yr were recorded in the Setiu beach ridge plain of Terrengganu, northeastern Peninsular Malaysia (Mallinson et al., 2014), and it is argued that recent variation in El Niño intensity and monsoon activity affect the sediment deposition regime on annual to interannual timescales.

At Chan May, the decline in coastal progradation may be linked to the transition from the inner 4.5 km wide embayment to the outer 6.5 km wide embayment (Fig. 1). Assuming that sediment supply has not varied, the wider outer embayment contains more space for sediments to accumulate, thereby slowing the rate of coastal progradation. Further declines in progradation rate since ca. 1.9 ka may be due to the prograded beach ridges having reached their maximum oceanward extent as controlled by the western headland (e.g. Oliver et al., 2019), declining and stabilizing sea levels (e.g. Ta et al., 2002), rising sea levels (Sharples et al., 2020) and variable climate (e.g. Mallinson et al., 2014; Sloss et al., 2018) may also have contributed to variable rates of progradation at Chan May. However, it is not possible at present to ascribe the degree of contribution of each of these factors.

It is likely that beach progradation in the western portion of the embayment will now cease and excess sediment will continue to, and very likely, rapidly fill the eastern portion of the embayment where accommodation space remains and change the orientation of the modern beach. Importantly, this location is where a deep-water port has been recently constructed (Fig. 1).

7.3. Recent coastal change

The modern coastal environment is characterized by similarly prograding beach face facies (Fig. 8), but that has been significantly affected by heavy mineral mining and subsequent rehabilitation (Lee et al., 2012, 2013). The heavy mineral mining and infilling of the mined areas occurred sometime between April 2003 and February 2009 as observed in historical Google Earth Satellite imagery (GoogleEarth, 2019). Prior to the heavy mineral mining, the backbeach

area had a covering of grass and sparse shrubs occurred on exposed sandy patches. These sandy patches may have formed a low elevation, aeolian re-worked beach ridge cap. Approximately 450 m inland of the vegetated edge of the modern beach a narrow, sparsely vegetated transgressive dune exists (Fig. 1). After heavy mining ceased the area was refilled with sand in a rehabilitation effort (Lee et al., 2012, 2013). Approximately 350 m of exposed flat sand provided sufficient fetch for wind to entrain sand, and vertically build and steepen the transgressive dune (Fig. 7). The morphology of the transgressive dune behind this rehabilitated area is vastly different from the same transgressive dune structure 430 m to the west that did not have the stoss-side of the landscape mined (Fig. 6).

At both locations, the transgressive dune occurs encroaching upon the most recent observable swale (Figs. 6 and 7). Underlying the transgressive dune are trough-shaped reflections inferred to be palaeo-drainage channels. The termination of the shallowest palaeochannels (ca. −2 m pmsl) may have occurred when the Bulu River breached the beach ridge system in the west of the Chan May Embayment resulting in the blockage of eastward flow in these palaeochannels. In agreement with Shepherd (1991) the development of foredunes is coincident with the decreasing rate of coastal progradation and increased wind supply of sand to the tops of the beach ridge. During rapid coastal progradation there is insufficient time for high foredunes to form, and the backshore is cut-off from the potential sand sources on the beach by new beach ridges (Shepherd, 1991). However, once the location of the beach is stabilized this gives time for sand to blow inland and coastal foredunes to develop (Shepherd, 1991; Psuty, 1992; Otvos, 2000).

7.4. River change

The Bulu River drains the swales and cuts across most of the beach ridges. The river begins as a narrow swale-draining channel that widens as the channel meanders towards the modern coastline. In the centre of Chan May, numerous cut-off or infilled meanders exist (Fig. 1). A long series of scroll bars (ca. 1.7 km) began forming at ca. 2 ka (OSL1, OSL2 and OSL4) and had prograded approximately 520 m rapidly.

Upstream of the scroll bars, a large floodplain (in places ca. 970 m wide) exists that is currently incised by the much narrower (ca. 50 m wide) Bulu River. The disproportionate size of the floodplain and scroll bar system defines the modern Bulu River as an underfit stream. The former Bulu River channel (Fig. 3) was in places 200 m wide and 7 m deep with well-defined meanders as evidenced by the epsilon cross beds within the channel (e.g. Collinson, 1996).

The underfit stream implies a sudden and significant decrease in the discharge of the Bulu River upstream of the scroll bars. The cause of this discharge decline is likely a 1.3 km long, 110 m wide straight section of river that cuts across the beach ridges in the north-central part of the strandplain and rejoins the primary Bulu River channel tangential to the northwestern side of the scroll bars (Fig. 1). Examination of historical maps of the region (Schweyer, 2016; www.pascha.human.org) suggest that this cut was made prior to 1875 and may have been in existence prior to 1630–1655 CE (Fig. 11a, b, c). It is unclear when this artificial cut was made, but extensive modifications of coastal barriers in the Hue Estuary during the 16th and 17th Centuries suggest extensive human modification of the coastal system in this period (Schweyer, 2016).

7.5. Storm records from GPR

Two forms of storm deposits are observed in the GPR profiles and demonstrate that the Chan May embayment has been repeatedly struck by typhoons throughout the Holocene sea-level regressive phase.

The first and most common indicators of palaeostorm events are beach and shoreface clinoforms that have been truncated at a steeper angle, forming erosional scarps (Figs. 4 and 7; e.g. Bristow et al., 2000; Buynevich et al., 2007, 2011; Pile et al., 2016; Liu et al., 2016; Tamura et al., 2019b). Often, the erosional surface has short, onlapping reflections at depths of −1 to −3 m, that are interpreted as landward migrating swash bars in the upper shoreface. The truncation surfaces are inferred to be the result of storms eroding the beachface and depositing sediments below the shoreface in offshore bars. Following the storm, fair-weather wave conditions then rebuild the beach through swashbar migration. Similar storm erosional and recovery packages have been observed in Guichen Bay, South Australia (Bristow and Pucillo, 2006), Norfolk, UK (Bristow et al., 2000), Denmark (Clemmensen and Nielsen, 2010) and New South Wales (e.g. Tamura et al., 2019b).

The second type of palaeostorm indicator is a sequence of trapezoidal reflections containing steeply, inland-inclined reflections likely representing the terminal foresets of storm deposited washover fans (RF 7; e.g. Schwartz, 1975). These are only found above an infilled fluvial channel that lies beneath the modern transgressive dune (Fig. 6), and suggests that there was sufficient accommodation space to preserve the fans and that storm surge penetrated inland to deposit significant volumes of sediment. Similar radar facies and interpretations have been recognized in the USA (Wang and Horwitz, 2007), Peninsular Malaysia (Mallinson et al., 2014) and Brazil (Hein et al., 2013; Hein et al., 2016).

Wang and Horwitz (2007) also identified multiple trapezoidal structures with inclined tabular foresets that build inland and recognized these as part of Hurricane Ivan storm deposition. Anecdotal evidence from a Canh Duong village elder suggested a storm surge prior to 1940 had inundated and deposited sediment and pumice as far inland as the coastline edge of the transgressive dune. The modern quartz OSL age for the landward trapezoidal package (RF7, Fig. 6) observed in the GPR image may reflect this storm event. Either way, the geomorphological and geophysical evidence presents a dramatic change form a long term progradational record over the past 6000 years to one of aggradation, with washovers and transgressive dune development that is likely to be a response to a switch in the balance between accommodation space and sea-level change (e.g. Sharples et al., 2020).

8. Conclusion

Infill of the Chan May embayment in central Vietnam is recorded by a series of beach ridges that mark the successive position of the coastline. Dating of the beach ridge sequence indicates that the coastal plain at Chan May has accumulated since the Mid-Holocene, 5000–6000 years ago. Initial rates of progradation were relatively rapid, around 2.3 to 2.7 m/yr, between 6000 and 4000 years ago, but from 4000 to 2000 years ago the rate of progradation almost halved to 1.3–1.5 m/yr. In the past 2000 years, the progradation rate halved again to 0.6–0.7 m/yr. The latest reduction in progradation rates appears to be associated with a change in the beach ridge dynamics and the development of coastal dunes. It is likely that the Holocene progradation has been forced by a fall in relative sea level over the past 6000 years and changes in the available accommodation space in the coastal zone. Looking ahead, it is possible that the Holocene coastal progradation has run its course and will now cease. This may result in widespread changes in coastal dynamics and a switch from historical progradation across the entire beachfront to coastal stabilization in the western margin and rapid infilling and changed beach orientation in the east where a deepwater port has been constructed. With future sea level rise, aggradation or erosion and retreat may begin to occur. Ongoing coastal development within Vietnam and along the coast of Southeast Asia needs to be set within this context with increasing demands for coastal resources and a limited sediment supply that might already be insufficient to keep pace with sea-level change.

Declaration of competing interests

The authors declare that they have no known competing financial interests or personal relationships that could have appeared to influence the work reported in this paper.

Acknowledgements

This research is supported by the NUS Grant (R: 109-000-233-133) awarded to C.G. and the Singapore National Research Foundation fellowship scheme (Grant No: NRF-RF2010-04) awarded to A.D.S. We thank Anne-Valérie Schweyer for the historical maps. This paper is EOS contribution 303 and a contribution to IGCP639 "Sea Level Change: Minutes to Millennia". We also thank Toru Tamura and two anonymous reviewers for their constructive reviews which vastly improved the manuscript.

References

Bristow, C.S., Pucillo, K., 2006. Quantifying rates of coastal progradation from sediment volume using GPR and OSL: the Holocene fill of Guichen Bay, south-east South Australia. Sedimentology 53, 769–788.

Bristow, C.S., Chroston, P.N., Bailey, S.D., 2000. The structure and development of foredunes on a locally prograding coast: insights from ground-penetrating radar surveys, Norfolk, UK. Sedimentology 47, 923–944.

Buynevich, I.V., FitzGerald, D.M., Goble, R.J., 2007. A 1500 yr record of North Atlantic storm activity based on optically dated relict beach scarps. Geol. 35, 543–546.

Buynevich, I.V., Klein, H.F., FitzGerald, D.M., Cleary, W.J., Hein, C., Veiga, F., Angulo, R.J., Asp, N.E., Petermann, R.M., 2011. Geological legacy of storm erosion along a high-energy indented coastline: northern Santa Catarina, Brazil. J. Coast. Res. SI 64, 1840–1844 (Proceedings of the 11th International Coastal Symposium), Poland.

Clemmensen, L.B., Nielsen, L., 2010. Internal architecture of a raised beach ridge system (Anholt, Denmark) resolved by ground-penetrating radar investigations. Sediment. Geol. 223, 281–290.

Collinson, J.D., 1996. Alluvial sediments. In: Reading, H.G. (Ed.), Sedimentary Environments: Processes, Facies and Stratigraphy, 3rd edition Blackwell Publishing, Sydney, Australia, pp. 37–82.

Cunningham, A.C., Bakker, M.A.J., van Heteren, S., van der Valk, B.V., van der Spek, A.J.F., Schaart, D.R., Wallinga, J., 2011. Extracting storm-surge data from coastal dunes for improved assessment of flood risk. Geol. 39, 1063–1066.

Digital Typhoon, 2019. http://agora.ex.nii.ac.jp/cgi-bin/dt/search_name2.pl?gid=aa2d9650a02d57263ffd6f6bcaf409b7andlang=enandbasin=wnp/, Accessed date: 31 July 2019.

Do, A.T.K., de Vries, S., Stive, M.J.F., 2018. Beach evolution adjacent to a seasonally varying tidal inlet in Central Vietnam. J. Coast. Res. 34, 6–25.

GoogleEarth, 2019. Google Earth Pro 7.3.2.5776. (October 5, 2019). *Chan May Region, Hue Province, Vietnam*. 16°18′44.64"N, 107°59′16.30"E, Eye alt 36 mi. Borders and labels; places layers. Image Maxar Technologies 2020, Image NASA. <http://www.google.com/earth/index.html> (Accessed February 20, 2020).

Goscha, C., 2016. Vietnam: A New History. Basic Books, New York, USA 592 pgs.

Gouramanis, C., Switzer, A.D., Polivka, P., Bristow, C.S, Jankaew, K., Pham, T.D., Lee, Y.S., Rubin, C., Ramos, I.S., 2015. Ground Penetrating Radar examination of thin tsunami beds – A case study from Phra Thong Island, Thailand. Sediment. Geol. 329, 149–165.

Guérin, G., Mercier, N., Adamiec, G., 2011. Dose-rate conversion factors: update. Ancient TL 29, 5–8.

Hanebuth, T.J.J., Stattegger, K., Grootes, P.M., 2000. Rapid flooding of the Sunda Shelf: A late-glacial sea-level record. Science 288, 1033–1035.

Hayton, B., 2010. Vietnam: Rising Dragon. Yale University Press, London, UK 272 pgs.

Hein, C.J., FitzGerald, D.M., Cleary, W.J., Albernaz, M.B., de Menezes, J.T., Klein, A.H.D.F., 2013. Evidence for a transgressive barrier within a regressive strandplain system: implications for complex coastal response to environmental change. Sedimentology 60, 469–502.

Hein, C.J., FitzGerald, D.M., de Souza, L.H.P., Georgiou, I.Y., Buynevich, I.V., Klein, A.H.D.F., de Menezes, J.T., Cleary, W.J., Scolaro, T.L., 2016. Complex coastal change in response to autogenic basin infilling: an example from a sub-tropical Holocene strandplain. Sedimentology 63, 1362–1395.

Hoang, V.H., 2012. Housing and climate change: adaptation strategies in Vietnam. In: Yuen, B., Kumssa, A. (Eds.), Climate Change and Sustainable Urban Development in Africa and Asia. Springer, New York, pp. 167–192.

IPCC, 2019: Summary for policymakers. In: IPCC Special Report on the Ocean and Cryosphere in a Changing Climate [H.-O. Pörtner, D.C. Roberts, V. Masson-Delmotte, P. Zhai, M. Tignor, E. Poloczanska, K. Mintenbeck, M. Nicolai, A. Okem, J. Petzold, B. Rama, N. Weyer (eds.)]. In press.

Jevrejeva, S., Jackson, L.P., Riva, R.E., Grinsted, A., Moore, J.C., 2016. Coastal sea level rise with warming above 2 °C. Proc. Natl. Acad. Sci. 113, 13342–13347.

Joint Typhoon Warning Centre, 2019. https://www.metoc.navy.mil/jtwc/jtwc.html?western-pacific/, Accessed date: 31 July 2019.

Jol, H.M., Bristow, C.S., 2003. GPR in sediments: advice on data collection, basic processing and interpretation, a good practice guide. In: Bristow, C.S., Jol, H.M. (Eds.), Ground Penetrating Radar in Sediments. Geol. Soc. Lond., Spec. Publ. 211, 9–27.

Lee, Y.S., Gouramanis, C., Switzer, A.D., Bristow, C.S., Soria, J.L., Pham, T.D., Hoang, Q.D., Dinh, L.D., 2012. Ground penetrating radar (GPR) survey of formerly mined coastal dunes in central Vietnam: a rapid, non-invasive method for investigating the extent and impact of mined areas. Proc. Annu. Int. Conf. Geol. Earth Sci. 1–6 (GEOS 2012).

Lee, Y.S., Gouramanis, C., Switzer, A.D., Bristow, C.S., Soria, J.L., Pham, T.D., Hoang, Q.D., Dinh, L.D., 2013. Ground Penetrating Radar (GPR) survey of formerly mined coastal dunes in central Vietnam: a rapid, non-invasive method for investigating the extent and impact of mined areas. J. Geol. Earth Sci. 1, 11–19.

Liu, Y., Huang, H., Qi, Y., Liu, X., Yang, X., 2016. Holocene coastal morphologies and shoreline reconstruction for the southwestern coast of the Bohai Sea, China. Quat. Res. 86, 144–161.

Mallinson, D.J., Smith, C., Mahan, S., Culver, S., McDowell, K., 2011. Barrier island response to Late Holocene climate events, North Carolina, USA. Quat. Res. 76, 46–57.

Mallinson, D.J., Culver, S.J., Corbett, D.R., Parham, P.R., Shazili, N.A.M., Yaacob, R., 2014. Holocene coastal response to monsoons and relative sea-level changes in northeast peninsular Malaysia. J. Asian Earth Sci. 91, 194–205.

Neal, A., 2004. Ground-penetrating radar and its use in sedimentology: principles, problems, and progress. Earth-Sci. Rev. 66, 261–330.

Neumann, B., Vafeidis, A.T., Zimmermann, J., Nicholls, R.J., 2015. Future coastal population growth and exposure to sea-level rise and coastal flooding — a global assessment. PLoS One 10 (3), e0118571.

Nghiem, T.L., 2009. Hydrodynamics and Morphodynamics of a Seasonally Forced Tidal Inlet System. Unpub thesis, p. 148.

Nguyen, V.L., Ta, T.K.O., Tateishi, M., 2000. Late holocene depositional environments and coastal evolution of the Mekong River Delta, Southern Vietnam. J. Asian Earth Sci. 18, 427–439.

Nguyen, V.L., Ta, T.K.O., Saito, Y., 2010. Early Holocene initiation of the Mekong River delta, Vietnam, and the response to Holocene sea-level changes detected from DT1 core analyses. Sediment. Geol. 230, 146–155.

Nielsen, L., Bendixen, M., Kroon, A., Hede, M.U., Clemmensen, L.B., Weβling, R., Elberling, B., 2017. Sea-level proxies in Holocene raised beach ridge deposits (Greenland) revealed by ground-penetrating radar. Sci. Rep. 7, 46460. https://doi.org/10.1038/srep46460.

Nott, J., 2019. Discussion of 'Coarse-sand beach ridges at Cowley Beach,north-eastern Australia: Their formative processes andpotential as records of tropical cyclone history' by Tamura et al.(2018),Sedimentology, 65, 721–744. Sedimentology 66, 764–768.

Nott, J., Goff, J., Change-Goff, C., Sloss, C., Riggs, N., 2013. Anatomy of sand beach ridges: evidence from severe Tropical Cyclone Yasi and its predecessors, northeast Queensland, Australia. J. Geophys. Res. Earth Surf. 118, 1–10.

Oliver, T.S.N., Tamura, T., Short, A.D., Woodroffe, C.D., 2019. Rapid shoreline progradation followed by vertical foredune building at Pedro Beach, southeastern Australia. Earth Surf. Process. Landforms 44, 655–666.

Otvos, E.G., 2000. Beach ridges — definitions and significance. Geomorphology 32, 83–108.

Pacha Hum-an Project, 2019. http://pacha.huma-num.fr/en/resultats-du-projet/evolution-des-ouvertures-sur-la-mer/, Accessed date: April 2019.

Pile, J., Switzer , A.D., Soria, L., Siringan, F., Daag, A., 2016. An investigation of recent storm histories using Ground Penetrating Radar at Bay-Bay Spit, Bicol, Central Philippines. 16th International Conference of Ground Penetrating Radar (GPR) 4 pages.

Pile, J., Gouramanis, C., Switzer, A.D., Rush, B., Reynolds, I., Soria, J.L.A., 2018. Can the risk of coastal hazards be better communicated? Int. J. Dis. Risk Red. 27, 439–450.

Pile, J., Cooper, J.A.G., Jackson, D.W.T., 2019. Stratigraphy and internal structure of wind-dominated barrier islands (dune and machair) of the Outer Hebrides, Scotland. Earth Surf. Process. Landf. 44, 1482–1493.

Psuty, N.P., 1992. Spatial variation in coastal foredune development. In: Carter, R.G.W., Curtis, T.G.F., Sheehy-Skeffington, M.J. (Eds.), Coastal Dunes. Balkema, Rotterdam, pp. 3–13.

Sánchez-Arcilla, A., García-León, M., Gracia, V., Devoy, R., Stanica, A., Gault, J., 2016. Managing coastal environments under climate change: Pathways to adaptation. Sci. Total Environ. 572, 1336–1352.

Schimanski, A., Stattegger, K., 2005. Deglacial and Holocene evolution of the Vietnam shelf: stratigraphy, sediments and sea-level change. Mar. Geol. 214, 365–387.

Schwartz, R.K., 1975. Nature and genesis of some storm washover deposits. Mem. coastal. Engrg. Res. Cent. Tech. 61, 69.

Schweyer, A.-V., 2016. Exploitation of a historical geographic information system (GIS) in Thua Thiên-Hue and Quang Tri provinces, Central Vietnam. In: Tan, N.H. (Ed.), Selected Papers from the Second SEAMEO SPAFA International Conference on Southeast Asian Archaeology, pp. 227–235.

Sharples, C., Walford, H., Watson, C., Ellison, J.C., Hua, Q., Bowden, N., Bowman, D., 2020. Ocean Beach, Tasmania: a swell-dominated shoreline reaches climate induced recessional tipping point? Mar. Geol. 419, 106081.

Shepherd, M.J., 1991. Relict and contemporary foredunes as indicators ofcoastal processes. In: Brierley, G., Chappell, J. (Eds.), Applied Quaternary Studies. Australian National University, Canberra, Australia, pp. 17–24.

Simms, A.R., Regina DeWitt, R., Zurbuchen, J., Vaughan, P., 2017. Coastal erosion and recovery from a Cascadia subduction zone earthquake and tsunami. Mar. Geol. 392, 30–40.

Sloss, C.R., Nothdurft, L., Hua, Q., O'Connor, S.G., Moss, P.T., Rosendahl, D., Petherick, L.M., Nanson, R.A., Mackenzie, L.L., Sternes, A., Jacobsen, G.E., Ulm, S., 2018. Holocene Sea-level change and coastal landscape evolution in the southern Gulf of Carpentaria, Australia. The Holocene 28, 1411–1430.

Sterling, E.J., Hurley, M.M., Minh, L.D., 2006. Vietnam: A Natural History. Yale University Press pgs 423.

Switzer, A.D., Gouramanis, C., Inggrid, M.I., Bristow, C.S., Jol, H.M., Simms, A.R., 2020. Ground-penetrating radar (GPR) in coastal hazard studies: theories, issues and potential. In: Engel, M., Pilarczyk, J., May, S., Brill, D., Garrett, E. (Eds.), Geological Records of Tsunamis and other Extreme Waves.

Ta, T.K.O., Nguyen, V.L., Tateishi, M., Kobayashi, I., Saito, Y., 2002. Holocene delta evolution and sediment discharge of the Mekong River, southern Vietnam. Quat. Sci. Rev. 21, 1807–1819. https://doi.org/10.1016/S0277-3791(02)00007-0.

Ta, T.K.O., Nguyen, V.L., Tateishi, M., Kobayashi, I., Saito, Y., 2005. Holocene delta evolution and depositional models of the Mekong River delta, southern Vietnam. In: Giosan, L., Bhattacharya, J.P. (Eds.), River deltas—Concepts, models, and examples. 83. Society for Sedimentary Geology Special Publication, pp. 453–466.

Tamura, T., 2012. Beach ridges and prograded beach deposits as palaeoenvironment records. Earth-Sci. Rev. 114, 279–297.

Tamura, T., Murakami, F., Nanayama, F., Watanabe, K., Saito, Y., 2008. Ground-penetrating radar profiles of Holocene raised-beach deposits in the Kujukuri strand plain, Pacific coast of eastern Japan. Mar. Geol. 248, 11–27.

Tamura, T., Saito, Y., Nguyen, V.L., Ta, T.K.O., Bateman, M.D., Matsumoto, D., Yamashita, S., 2012. Origin and evolution of interdistributary delta plains; insights from Mekong River delta. Geology 40, 303–306.

Tamura, T., Nicholas, W.A., Oliver, T.S., Brooke, B., 2018. Coarse-sand beach ridges at Cowley Beach, North-Eastern Australia: their formative processes and potential as records of tropical cyclone history. Sedimentology 65, 721–744.

Tamura, T., Nicholas, W.A., Oliver, T.S., Brooke, B., 2019a. Reply to the Discussion of John Nott on 'Coarse-sand beach ridges at Cowley Beach, North-Eastern Australia: their formative processes and potential as records of tropical cyclone history by Tamura et al. (2018), Sedimentology, 65, 721–744'. Sedimentology 66, 769–773.

Tamura, T., Oliver, T.S.N., Cunningham, A.C., Woodroffe, C.D., 2019b. Recurrence of extreme coastal erosion in SE Australia beyond historical timescales inferred from beach ridge morphostratigraphy. Geophys. Res. Lett. 46, 4705–4714.

Tanabe, S., Saito, Y., Vu, Q.L., Hanebuth, T.J.J., Ngo, Q.L., Kitamura, A., 2006. Holocene evolution of the Song Hong (Red River) delta system, northern Vietnam. Sediment. Geol. 187, 29–61.

Tanaka, G., Komatsu, T., Saito, Y., Nguyen, D.P., Vu, Q.L., 2011. Temporal changes in ostracod assemblages during the past 10,000 years associated with the evolution of the Red River delta system, northeastern Vietnam. Mar. Micropaleontol. 81, 77–87.

Taylor, M., Stone, G.W., 1996. Beach-ridges: a review. J. Coast. Res. 12, 612–621.

Thao, N.V., Thanh, T.D., Saito, Y., Gouramanis, C., 2013. Monitoring coastline change in the Red River Delta using remotely sensed data. J. Mar. Science and Tech. 13, 151–160.

TPCTTHP, (n.d.) Khu Kinh Te: Chan May-Lang Co Economic Zone. The People's Committee of Thua Thien Hue Province. 9 pgs.

Wang, P., Horwitz, M.H., 2007. Erosional and depositional characteristics of regional overwash deposits caused by multiple hurricanes. Sedimentology 54, 545–564.

Wang, S.S.-Y., Promchote, P., Truong, L.H., Buckley, B., Li, R., Gillies, R., Trung, N.T.Q., Guan, B., Minh, T.T., 2015. Changes in the autumn precipitation and tropical cyclone activity over Central Vietnam and its East Sea. Viet. J. Earth Sci. 36, 1–7.